University of Genoa

Master Thesis

Fiber Tracking Velocimetry

Author:
Stefano Brizzolara

Supervisors:
Prof. Dr. Andrea Mazzino
Prof. Dr. Markus Holzner
M. Sc. Giorgia Tagliavini
M. Sc. Marius Neamtu Halic

Master degree

in

Civil and Environmental Engineering
Department of Civil, Chemical and Environmental Engineering

November 8, 2019

UNIVERSITY OF GENOA

Abstract

Faculty of Engineering
Department of Civil, Chemical and Environmental Engineering

Master

Fiber Tracking Velocimetry

by Stefano Brizzolara

This project is developed with the Environmental Fluid Mechanics Group of Prof. Markus Holzner[1] at ETHZ[2] supervised by Prof. Andrea Mazzino[3], that had the main theoretical original ideas behind it. The main goals is to experimentally investigate the behaviour of small polymeric fibers flapping in a turbulent flow. To do so it is necessary to develop a method to hand-craft the fibers and to make them traceable by means of photogrammetry techniques.

The focus will be on the behaviour of rigid fibers flapping and spinning in turbulence and on how it is possible to measure some two-points suitable statistical properties of turbulence by means of these fibers. A phenomenological theory had already been developed for flexible fibers and some proofs had been founded by means of direct numerical simulation; no theory or evidences have been found about rigid fibers.

It will be shown that, by tracking rigid fibers in a turbulent flow, it is possible to measure transverse velocity differences and eddies tumbling time at the scale of the length of the fiber; this leads to develop a new experimental technique in turbulence measuring that we called Fiber Tracking Velocimetry (FTV): instead of spreading particles in a turbulent flow and measuring velocity differences considering particle couples, it is possible to spread some fibers of different length and measure velocity differences at the capes of the fibers.

[1]Senior Scientist at Eidg. Forschungsanstalt für Wald, Schnee und Landschaft, WSL and Assistant Professor of Environmental Fluid Mechanics, ETH Zurich

[2]Swiss Federal Institute of Technology in Zurich

[3]associate professor at DICCA, University of Genoa

Contents

List of Figures

List of Tables

Chapter 1

Introduction

The main reasons that leaded to develop this thesis are reported also by showing some examples related to measured flow fields. Moreover the goals of this work are setted.

1.1 Motivations

Why the study of turbulence is still important? Undoubtedly, turbulence related phenomena are present in many aspects of our life. The smoke coming out of a chimney is a turbulent flow [2], as well as the dynamic of sea wave breaking on a sea wall [3]; but also weather forecast implies the need of turbulence modelling [4], as well as the flow in a turbine [5]; the motion of a cigarette smoke is turbulent. Moreover and more surprisingly van Gogh paintings[6] show typical turbulent patterns that follows turbulence physical laws.

From an environmental engineering point of view, the study of turbulence is central in most of the subject topics; indeed, turbulence concerns fluid dynamic across the scales: turbulence theory can describe the fluid flow in an aorta [7] as well as Rossby waves [8] that are at a planetary scale.

Nevertheless, studying turbulence symmetries and scaling properties is even more beautiful than important. Turbulence induces the scientists to think that a universal law that rules the fluid motion exists [9] [10] [11], and this is extremely intriguing for a scientific mind.

We propose a new technique for measuring turbulence In this work, we propose an innovative approach to measure two points statistical properties of turbulence. In fact, the foundamental idea is to measure flow fields by means of fibers (slender bodies) instead of tracers (particles, puntual objects). Indeed, we believe that, under certain conditions, a fiber can caputure the behaviour of turbulent eddies characterized by its length scale, and therefore that the fiber motion is slved to the turbulence forcing.

More in detail, at the state of the art, one of the most used methodology to measure turbulent flow field is Particle Tracking Velocimetry (PTV) [12]; it consists in spreading 0-D objects (particles) in the flow and tracking their position in time; the word "particles", in general, refers to an object characterized by a size that is much smaller than the scale of the considered problem: this means that, if a micro-fluid device is considered, "particles" means spheres with a diameter of less than $10\,\mu m$; if we consider oceanographic large scale measurements, an instrumented oceanographic float can be considered as a punctual object [13]. Under certain conditions, the particles remain attached to the fluid elements and behave just like them. This condition is essentially related to the time with which a particle responds to the fluid force acting on it: if the particle reacts instantaneously, i.e. without delays respect to the fluid element, it will follow the flow.

Our idea comes from the following conjecture: the edges of an 1-D element (the fiber) will move, from a statistical point of view, such as the surrounding fluid; this helps the scientists in "keeping couples of particles" (the fibers edges) at a circumscribed distance letting their dynamical behaviour to be still "slaved to turbulence". Therefore, it would be possible to measure continuously in time the dynamics of two particles at a fixed distances (the fiber edges) without them to be spread because of the turbulence diffusivity.

What is the importance of our new approach? The idea of "connected particles couples" comes from the following knowledge: in most of the cases, turbulence presents a diffusive behaviour, i.e. two particles released in a turbulent flow will increase their distance since their velocity are not correlated anymore [14] [15]. This means that the main problem when using tracers to access Eulerian statistics of turbulence is that particles tend to separate from each other by virtue of the so called Richardson law that states that the diffusivity increases as the 2/3 power of the particles cluster width. This phenomena prevents obtaining converged statistics for a given fixed separation between the particle, since they quickly lose their correlation.

To persuade the reader of this argumentation, a couple of real life example is presented. In Figure 1.1 a radar measurement of the unsteady surface flow field in front of the Gulf of Trieste is shown. The data are kindly provided by Prof. Marcello Magaldi[1] during the lectures of *Dispersion Processes* at the university of Genoa[2]. A cluster of neutral floats is released on the flow field in the center of the domain with a small initial separation distance and then their Lagrangian trajectories are evaluated solving the following differential equations with a RK4 explicit method:

$$\frac{dx_i}{dt} = u(x_i, y_i), \quad \frac{dy_i}{dt} = v(x_i, y_i) \tag{1.1}$$

where (x_i, y_i) are the coordinates of the i^{th} float; the separation distance between two floats is evaluated as:

$$r = \sqrt{(x_2 - x_1)^2 + (y_2 - y_1)^2} \tag{1.2}$$

In Figure 1.1(a) the initial (black bullets) and final (red bullets) position of the floats is shown. It is clear that the cluster disperses completely all over the gulf. The floats cluster size increases quasi monotonically in time, as shown in Figure 1.1(b): after a short period of less then one day in which r remains almost the same, therefore it increases indefinitely. This example highlights the fact that turbulence spread the particles leading them to be decorrelated and, as mentioned above, the decorrelation leads to difficulties in having convergent statistics: this fact is not a problem since it is possible to spread a large number of particles at a fixed distance just like happens in a small scale laboratory experiment. Indeed, in a laboratory experiment, to spread four or five thousand of particles in a $10 \cdot 10 \cdot 10\,cm$ volume is matter of pushing a syringe for half a second; to spread some dozens of floats in the ocean at a fixed distance is matter of days and thousand Euros. Here it is the main advantages of this technique. More examples can be carried out, such as meso-scale atmospheric turbulence, or open channel surface turbulence.

[1] CNR-ISMAR researcher
[2] UNIGE University of Genoa

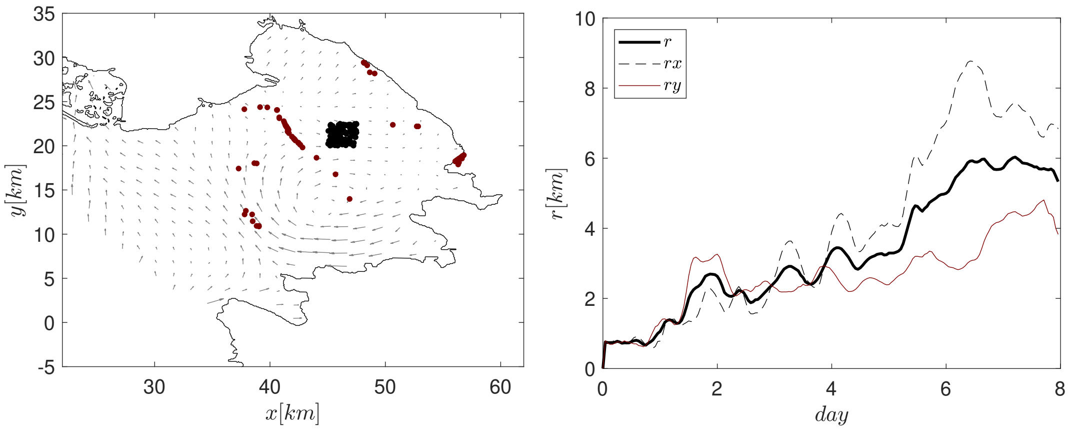

(a) trajectories (b) separation

FIGURE 1.1: Radar data of the surface flow field in the gulf of Trieste.

Even if the advantages of using fibers instead of tracers to measure the statistical properties of the flow field is more evident at synoptic scales, it is possible to use them in a laboratory set-up; the advantages are not directly related to the diffusive behaviour of turbulence, but, as will be shown through this work, to have a direct measure of some observable that are particularly hard to measure with tracers, such as the eddies tumbling time.

In Figure 1.2 a similar example done on a 3-D flow field is shown; a cluster of 200 passive particles is released in a turbulent flow that I measured in laboratory with 3-D particle tracking (3-D PTV) techniques. The particles are released on the flow field and their position had been evaluated solving the 3-D version of equation (1.1); in Figure 1.2(a) the position of the cluster is shown at the initial time (black) and after $0.25\,s$ (red), where $0.25\,s$ is a large eddy turnover time. In Figure 1.2(b), the average distance between the particles in the cluster is shown; the average separation increases almost monotonically in time. The diffusive behaviour of turbulence is more evident in the second case, since the smaller scales of the field are better resolved; in fact, the smaller scales are responsible of the diffuse behaviour of turbulence; the flow field at large scales tend to move the passive scalar fields without spreading it.

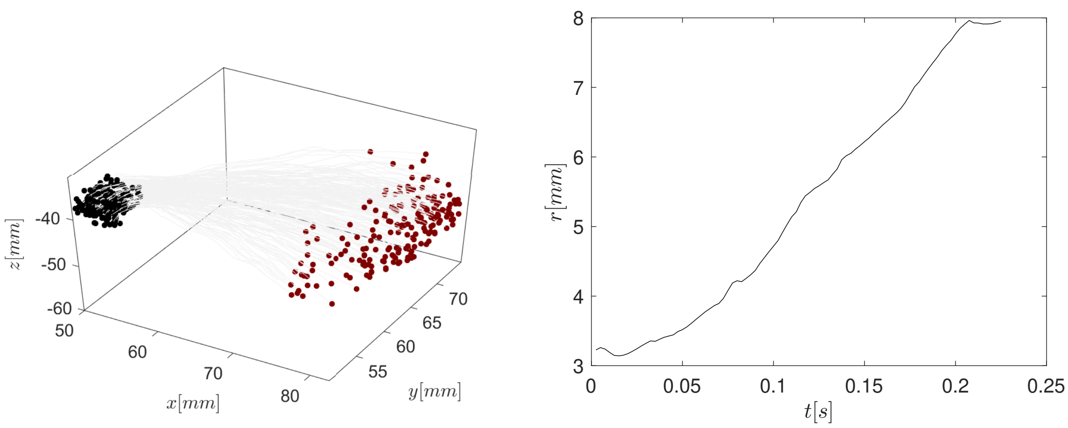

(a) trajectories (b) average separation

FIGURE 1.2: Particles dispersion in 3-D turbulence.

1.2 Goals

The main goal of the project is to measure some turbulence statistical properties in the laboratory controlled environment, with our new approach and another reliable technique, so that a comparison between the two methodology can be done. The key steps of the project are the following:

1. develop a method to cast small sized polymeric fibers that can be tracked by means of photogrammetry techniques in a turbulent flow;
2. recreate a controlled turbulent flow that can be characterized by means of 3-D particle tracking velocimetry;
3. develop a method to track the fibers while moving in turbulence;
4. investigate if it is possible to measure some suitable observables with the fibers.

This project involves different fields of knowledge: concerning the polymeric fibers hand-crafting, chemical processes and polymer mechanical properties has to be studied (polymerisation, relationship between the concentration of a part in a polymer solution and the mechanical features of the material, etcetera); regarding the problem of 3-D bodies freely moving in turbulence the fundamental physics of fluid-structure interaction problems has to be known (normal mode, viscous dumping, tumbling, etcetera); regarding the experimental measure of a fluid flow, photogrammetry has to be well understood (epipolar geometry, focal length, distortions, etcetera). Moreover a strong knowledge of computer coding is necessary to analyse the collected data.

Since the motion of a flexible fiber has been already investigated by means of direct numerical simulations [16] [17], this project is focused on the dynamics of rigid fibers. The main goal of the project consists in trying to show experimentally if a rigid fiber tumbles at the same frequency of the eddies of its length scale, and, if this is the fact, under which conditions this happens.

Chapter 2

Velocity differences and structure functions

Some useful results derived by Kolmogorov in 1941 are presented. Firstly, the energy spectrum equation, that describe the scale by scale energy balance is described; secondly, an overview of phenomenological laws resulting from the so called K41 theory are presented and discussed. Eventually, theory and experimental evidences about the longitudinal and transverse structure functions of turbulence are discussed deeper.

2.1 An overview of the energy spectrum equation

Let us assume that the fluid flow is governed by the incompressible Navier-Stokes equations. They represent the momentum and mass conservation of a viscous incompressible fluid element. In vectorial notation they are:

$$\frac{\partial \mathbf{u}}{\partial t} + \mathbf{u} \cdot \nabla \mathbf{u} = -\frac{1}{\rho} \nabla p + \nu \Delta \mathbf{u} + \mathbf{f} \tag{2.1}$$

$$\nabla \cdot \mathbf{u} = 0 \tag{2.2}$$

where $\mathbf{u} = (u, v, w)$ is the Eulerian velocity field, ρ is the fluid density, p is the pressure field and ν is the molecular viscosity. $\mathbf{f}$ is a force volume density. Moreover, the NS equations must be supplemented by initial and boundary condition, such as periodic boundary conditions or no-slip condition at rigid walls [18, Ch. 1].

To better formalize the familiar and useful concept of "scale" frequently employed in the phenomenological turbulence theory, a scalar function $f(\mathbf{x}, t)$ of both space and time can be considered. If f is $L-$*periodic* in space, it can be decomposed in its harmonic components using the Fourier series:

$$f(\mathbf{r}) = \sum_k \hat{f}_k e^{i\mathbf{k}\cdot\mathbf{r}}, \quad \mathbf{k} \in \frac{2\pi}{L} Z^3 \tag{2.3}$$

where $i^2 = -1$. Two functions can be defined depending on $K > 0$; the low pass and high pass filtered functions respectively:

$$f_K^{<}(\mathbf{r}) = \sum_{k \leq K} \hat{f}_k e^{i\mathbf{k}\cdot\mathbf{r}} \tag{2.4}$$

$$f_K^{>}(\mathbf{r}) = \sum_{k > K} \hat{f}_k e^{i\mathbf{k}\cdot\mathbf{r}} \tag{2.5}$$

and therefore, trivially:

$$f(\mathbf{r}) = f_K^{<}(\mathbf{r}) + f_K^{>}(\mathbf{r}) \tag{2.6}$$

By applying this filter operator to the k^{th} velocity component, two functions $u_K^{<}(\mathbf{r})$ and $u_K^{>}(\mathbf{r})$ are obtained. Usually, they are named *eddies larger/smaller than l* where $l = 1/K$ is the filtering scale.

By applying the low pass filter (2.4) on the NS equations and then taking the scalar product with the low pass filtered velocity $u_K^{<}(\mathbf{r})$, therefore averaging over the space coordinates ($\langle\cdot\rangle$), the scale by scale energy budget equation can be obtained:

$$\frac{\partial \mathcal{E}_K}{\partial t} + \Pi_K = -2\nu\Omega_K + \mathcal{F}_K \tag{2.7}$$

where:

$$\mathcal{E}_K = \frac{1}{2}\langle|\mathbf{u}_K^{<}|^2\rangle \tag{2.8}$$

is the cumulative energy between the wave numbers 0 and K,

$$\Omega_K = \frac{1}{2}\langle|\boldsymbol{\omega}_K^{<}|^2\rangle \tag{2.9}$$

is the cumulative enstrophy,:

$$\mathcal{F}_K = \langle \mathbf{f}_K \cdot \mathbf{u}_K^{<}\rangle \tag{2.10}$$

is the cumulative energy injection by the force f, and:

$$\Pi_K = \langle \mathbf{u}_K^{<} \cdot (\mathbf{u}_K^{<} \cdot \nabla \mathbf{u}_K^{>})\rangle + \langle \mathbf{u}_K^{<} \cdot (\mathbf{u}_K^{>} \cdot \nabla \mathbf{u}_K^{>})\rangle \tag{2.11}$$

Equation (2.7) represent how the energy rate of change at scales down to $l = 1/K$ (2.8) is equal to the energy injected at such scales by the forcing term (2.10), minus the energy dissipated at such scales (2.9), minus the flux of energy to smaller scales due to the non-linear interactions (2.11). Usually, at large Reynolds number, the energy injection is limited at large scales and the energy dissipation at small scales. It has to be noticed that the (2.7) holds under no assumption on the turbulence scenario. This equation is not representing the energy spectrum as it is written; further steps have to be done.

If we work with random homogeneous functions instead of periodic, the Fourier series can be replaced by Fourier transforms:

$$\mathbf{u}(\mathbf{r}) = \int_{\mathbb{R}^3} \hat{\mathbf{u}}_k e^{i\mathbf{k}\cdot\mathbf{r}} d^3k \tag{2.12}$$

$$\hat{\mathbf{u}}_k = \frac{1}{(2\pi)^3}\int_{\mathbb{R}^3} \mathbf{u}(\mathbf{r})\, e^{-i\mathbf{k}\cdot\mathbf{r}} d^3r \tag{2.13}$$

$$\mathbf{u}_K^{<}(\mathbf{r}) = \int_{|\mathbf{k}|<K} \hat{\mathbf{u}}_k e^{i\mathbf{k}\cdot\mathbf{r}} d^3k \tag{2.14}$$

In other world, to obtain the low pass filtered velocity field, the physical space functions have to be mapped in the frequency space (equation 2.13), then to be remapped in the physical space by considering only the scales greater than a threshold $l = 1/K$ (equation (2.14)).

We define the longitudinal velocity differences as:

$$\delta u_{\parallel} = (\mathbf{u}(\mathbf{x}+\mathbf{r}) - \mathbf{u}(\mathbf{x})) \cdot \frac{\mathbf{r}}{|\mathbf{r}|} \tag{2.15}$$

Under the assumption of isotropy and homogeneity, the statistical properties of the longitudinal velocity differences can be expressed as a function only of the length of the separation vector $r = |\mathbf{r}|$. The third order moment is defined as:

$$S_{\parallel}^{3}(r) = \langle \delta u_{\parallel}^{3} \rangle \tag{2.16}$$

It can be shown that, under the hypothesis of homogeneous and isotropic turbulence, the cumulative energy flux can be expressed as a function of the third order moment of the longitudinal velocity differences as:

$$\Pi_K = -\frac{1}{6\pi}\int_0^{\infty} \frac{Kr}{r}\left(1 + r\frac{\partial}{\partial r}\right)\left(3 + r\frac{\partial}{\partial r}\right)\left(5 + r\frac{\partial}{\partial r}\right)\frac{S_{\parallel}^{3}(r)}{r}dr \tag{2.17}$$

Eventually, by substituting k with K and taking the derivative of the (2.7) with respect to k, we can write the energy transfer relation for homogeneous and isotropic turbulence:

$$\frac{\partial E(k)}{\partial t} = T(k) + F(k) - 2\nu k^2 E(k) \tag{2.18}$$

where the energy spectrum is defined as:

$$E(k) = -\frac{\partial}{\partial k}\left(\frac{1}{2}\langle |\mathbf{u}_k^{<}|^2 \rangle\right) \tag{2.19}$$

The production term $F(k)$ is an an energy spectrum acting only near to a fixed (small) wave number, that is at the large integral scale:

$$F(k) = \frac{\partial}{\partial k}\left(\mathbf{f}_k^{<} \cdot \mathbf{u}_k^{<}\right) \tag{2.20}$$

The dissipation term $-2\nu k^2 E(k)$ is always negative; it is more relevant for large k, i.e. at small scales; $T(k)$ is called the transport term, and defined as:

$$T(k) = -\frac{\partial \Pi_k}{\partial k} \tag{2.21}$$

and therefore:

$$T(k) = \frac{1}{6\pi}\int_0^{\infty} cos(Kr)\left(1 + r\frac{\partial}{\partial r}\right)\left(3 + r\frac{\partial}{\partial r}\right)\left(5 + r\frac{\partial}{\partial r}\right)\frac{S_{\parallel}^{3}(r)}{r}dr \tag{2.22}$$

The denomination "transport term" is due to the fact that this term does not produce or dissipate energy. Indeed it can be proved that:

$$\int_0^{\infty} T(k)dk = 0 \tag{2.23}$$

The energy spectrum equation had been presented. The mathematical derivation is fully reported in [18, Ch. 2 and 6]. It is interesting to discuss its physical meaning and implication. The (2.18) can be seen as the energy balance in the range of scales from k to $k + dk$ and it is valid under the hypothesis of statistical homogeneity and isotropy of the turbulent field. The energy spectrum $E(k)$ is reduced from the dissipation term that is always negative since it is a negative quadratic form; the forcing term is always injecting energy; the transport term does not change the integral of the energy spectrum that means that it does not change the total amount of energy of the whole turbulent field. Nevertheless, it can, in principle, reduce or increase the rate of energy at the scale $l = 1/k$, sending energy to the larger or smaller scales. From the (2.22), it can be seen that the direction of the energy transfer depends on the sign of the third order moment.

2.2 The 4/5 law

Briefly spiking, the main theoretical result of the Kolmogorov turbulence theory consists of providing a non-trivial theoretical derivation of an expression for the third order structure function. This is an exact relationship between the third order moment of the longitudinal velocity increments, the length of the increments and the average turbulence dissipation rate.

In the following, the three Kolmogorov assumption under which the derivation of the 4/5 law has been carried out are listed and discussed; the 4/5 law is therefore enounced. The complete derivation of this relation is reported in [18, Ch. 6, sec. 2].

H1 : in the limit of infinite Reynolds number, all the possible symmetries of the Navier-Stokes equations, usually broken by the mechanisms producing the turbulent flow, are restored in a statistical sense at small scales and away from the boundaries. Small scales means $r \ll L$ where L is the integral scale, i.e. the scale at which the turbulence production takes place.

H2 : under the same assumption given in **H1**, the turbulent flow is self-similar at small scales, i.e. it possesses a unique scaling exponent $h \in R$ such that:

$$\delta\mathbf{u}\left(\mathbf{x}, \lambda\mathbf{r}\right) = \lambda^h \delta\mathbf{u}\left(\mathbf{x}, \mathbf{r}\right), \quad \forall h \in R_+ \tag{2.24}$$

for all $\mathbf{r}$ and $\lambda\mathbf{r}$ small compared to the integral scale.

H3 : under the same assumption given in **H1**, the turbulent flow has a finite non-vanishing mean rate of dissipation ϵ per unit mass.

Let us underline a non-trivial aspect: to reconcile the infinite Reynolds number hypothesis with the non vanishing turbulent dissipation rate leads to consider a vanishing viscosity. Indeed, by integrating the (2.18) and considering the (2.23), it can be shown that the turbulent dissipation rate must balance the production, that is:

$$\epsilon = \nu \left\langle \overline{\frac{\partial u_i}{\partial x_j}\frac{\partial u_i}{\partial x_j}} \right\rangle \sim \frac{U^3}{L} \tag{2.25}$$

where $\frac{U^3}{L}$ is obtained by dimensional argument combining the integral length scale with the integral velocity and it can be seen as an estimate of the production term, that, formally, is the integral over k of the 2.20. Usually, but not systematically, an estimate of the integral velocity can be given by:

$$U = u_{rms} \tag{2.26}$$

where:

$$u_{rms} = \sqrt{\langle u'^2 \rangle + \langle v'^2 \rangle + \langle w'^2 \rangle} \tag{2.27}$$

where $\langle \cdot \rangle$ is a suitable average and:

$$\mathbf{u}' = \mathbf{u} - \mathbf{U} \tag{2.28}$$

are the velocity fluctuations. The Reynolds number is defined from the integral scale quantities as:

$$Re = \frac{U \cdot L}{\nu} \tag{2.29}$$

To keep a non vanish dissipation rate the only way to increase the Reynolds number is decrease the fluid viscosity.

Under this three hypothesis, the Kolmogorov four-fifth law can be derived and provide an expression for the third order moment of the velocity differences at the separation r:

$$S_3(r) = -\frac{4}{5}\epsilon r \tag{2.30}$$

2.3 Implications and phenomenology

Three implications coming from the four-fifth law are stated and discussed. Firstly, the behaviour of turbulence within the inertial range is discussed; the energy spectrum is linked between the inertial range and the so called viscous range. Then, the concept of Richardson cascade is described. Eventually, an estimation of the amount of degrees of freedom necessary to describe a turbulent flow is derived.

The energy flows from large to small scales By substituting (2.30) in (2.17) and considering (2.18), it can be seen that, at least in 3-D turbulence, the transport term always decrease the amount of energy at the scale k, transferring energy from the wave number k to $k' > k$. In other words, the Kolmogorov $4/5$ law provide the energy flux direction. In analogy with thermodynamic, the energy balance can be seen as the first principle: without providing the second principle, it is not known if the heat transmits from higher temperature to low or vice versa. The $4/5$ law provide this criterion. Nevertheless, it is notable that by considering the 2-D NV equation and carrying out the same reasoning, the third order moment of the longitudinal velocity differences is positive: this is called inverse energy cascade, and can be seen experimentally [19].

Phenomenological implications From now on, the symbol $\sim$ will mean *equal within an order unity constant*; no distinction between vectors and their norm will be made. The $4/5$ law can be used to give an estimate of the velocity associated to the scale r within the inertial range:

$$u_r \sim \sqrt{\left(\langle \delta u_{\parallel}^2 \rangle\right)} \tag{2.31}$$

An estimation of the energy flux 2.22 can be provided combining the velocity at the scale r with r itself. Furthermore, the energy flux at every scales within the inertial range balances the dissipations:

$$\Pi_r \sim \frac{u_r^3}{r} \sim \epsilon \tag{2.32}$$

As it has been already shown in 2.25, it must happen also at the integral scale. This means that the production has to balance the dissipations. If we considered as integral scale velocity $U = u_{rms}$, if L is the integral length scale, we can write:

$$\frac{u_{rms}^3}{L} \sim \epsilon \tag{2.33}$$

that also can be seen as an estimate of the dissipations. Moreover, without bothering the $4/5$ law, the 2.32 provide a method to estimate the velocity increments or, roughly speaking, the velocity at the scale r:

$$u_r \sim \epsilon^{1/3} r^{1/3} \tag{2.34}$$

The eddies turnover time at the scale r inside the inertial range can be evaluated from the (2.34) as:

$$\tau_r \sim r u_r^{-1} \sim \epsilon^{-1/3} r^{2/3} \tag{2.35}$$

The bottom of the inertial range, where viscosity become relevant, can be obtained phenomenologically by considering the viscous time-scale, i.e. where r is the length scale at which the diffusion is significant:

$$\tau_{diff} \sim \frac{r^2}{\nu} \tag{2.36}$$

and comparing it with the eddies turnover time calculated as (2.35). It gives:

$$\eta = \left(\frac{\nu^3}{\epsilon}\right)^{1/4} \tag{2.37}$$

Equally, the time and velocity micro-scale can be obtained substituting (2.37) in (2.36) and (2.34):

$$\tau_\eta = \left(\frac{\nu}{\epsilon}\right)^{1/2} \tag{2.38}$$

$$u_\eta = (\nu\epsilon)^{1/4} \tag{2.39}$$

The Taylor length micro-scale is the intermediate length scale at which viscous dissipations significantly begin to affects the dynamics of the eddies. It can be evaluated by its definition or by the following expression [20, Ch. 6, Sec. 3]:

$$\lambda = \left(15\frac{\nu}{\epsilon}\right)^{1/2} u_{rms} \tag{2.40}$$

By a short manipulation, 2.40 can be also be used to estimate the turbulence dissipation rate. The corresponding Reynolds number is often used to characterized turbulent flows:

$$Re_\lambda = \frac{u_{rms}\lambda}{\nu} \tag{2.41}$$

Turbulence diffusive behaviour: the Richardson law As told before, the four-fifth law states that the third order moment of the longitudinal velocity differences is negative and provides a value for it. This fact means that the pdf of the longitudinal velocity differences is negatively skewed, i.e. is more probable to observe elongation of a fluid filament than shortening. Statistically speaking, it means that it is more likely to see two fluid elements increasing their distance in time than decreasing it. This can be practically seen spreading some tracer in a turbulent flow: the average distance between the particles increases in time. The diffusive behaviour of turbulence can be also be seen throw the Richardson law, that states that the relative diffusivity was scale-dependent. He found that the diffusivity increases as the point cloud width to the 4/3 power [15] [14].

Degrees of freedom of turbulence Combining (2.37) and (2.25) it is straightforward to derive the ratio between the integral scale and the Kolmogorov length microscale.

$$\frac{L}{\eta} = Re^{3/4} \tag{2.42}$$

In other words, the inertial range spance a range of scales that increases with the 3/4 power of the Reynolds number. If we want to describe a 3-D flow accurately on a uniform grid, the minimum number of grid points per integral scale that we need to describe all the turbulence eddies grows with its third power:

$$\#\left(dof\right) \sim \left(\frac{L}{\eta}\right)^3 \sim Re^{9/4} \tag{2.43}$$

Moreover, the time step with most of the numerical methods has to be proportional to the grid size. It can be shown that the total computational time required for each large eddy turnover time ($T = L/U$) increases as the third power of the Reynolds number.

2.4 Structure functions

The scaling properties of the longitudinal and transverse structure functions is discussed. A brief review about transverse structure function is presented, since it is not a direct implication of the Kolmogorov theory discussed above.

Longitudinal structure functions The scaling law for the longitudinal structure function is only known theoretically for the third order moment. As discussed above, in ideal conditions, the longitudinal velocity differences are characterized by a probability density function that is negatively skewed, e.g. the third order moment is always negative. Moreover, its scale law is known precisely, without scaling constants. From this result, it has been conjectured by dimensional arguments that:

$$S_{\parallel}^{p} = C_p \epsilon^{p/3} r^{p/3} \tag{2.44}$$

This is usually called 2/3 law, and it is observable form most of the turbulent flow if $Re >> 1$ [18, Ch. 5]. From an experimental point of view, it can be shown that:

$$S_{\parallel}^{2} = C_2 \epsilon^{2/3} r^{2/3} \tag{2.45}$$

where C_2 is called Kolmogorov constant and depends on the particular turbulence scenario. This means that $S_{\parallel}^{2} \sim r^{2/3}$ is easy to observe, but the multiplication constant change if the turbulence shows an anisotropic or non homogeneous behaviour.

It has to be noticed that to obtain the second order structure function is easier then the third order. In Figure 2.1, the second and the third order moment of data extracted randomly from a Gaussian distribution with 0 mean and 1 variance are shown: the convergence profile of the second order moment is clearly thinner then the third order one.

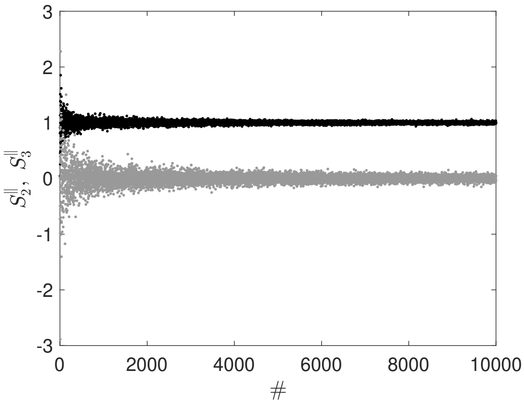

FIGURE 2.1: Second and third order moment of data sampled from a normal distribution with 0 mean and 1 variance against the dataset size.

Transverse structure functions The transverse velocity differences are the projection of the velocity difference onto a direction that is orthogonal to the separation. While the longitudinal direction is unique if two different points in space are considered, there exists infinite directions that are orthogonal to their orientation vector. Being $\mathbf{t}$ a unit vector such as $\mathbf{t} \cdot \mathbf{r} = 0$, the transverse velocity differences are defined as:

$$\delta u^{\perp} = \delta \mathbf{u} \cdot \mathbf{t} \tag{2.46}$$

The transverse structure function can be therefore defined as:

$$S_p^{\perp} = \langle \delta u_{\perp}^{p} \rangle \tag{2.47}$$

Different choices of $\mathbf{t}$ can be done: in [21], the transverse velocity differences are defined as:

$$\delta u_{\perp}\left(r\right) = |P\left(\frac{\mathbf{r}}{|\mathbf{r}|}\right) \delta \mathbf{u}\left(\mathbf{r}\right)| cos\left(\theta\right) \tag{2.48}$$

where:

$$P_{ij} = \delta_{ij} - \frac{r_i r_j}{r^2} \tag{2.49}$$

is a projection in the plane perpendicular to $\mathbf{r}$ and $\theta \in [0, 2\pi[$ is a random angle. This definition provide a good way to consider random direction orthogonal to $\mathbf{r}$; nevertheles, if we consider two fluid elements in a time interval for which they remain coherent, to extract this scalar quantity for each time-step produces a non continuous time signal.

In [22], transverse velocity differences are experimentally measured in a turbulent jet by means of RELIEF techniques. The x axis of the reference frame is oriented in the main jet direction; being the reproduced jet axial-symmetric, the choice of y is not relevant. The $u\left(y\right)$ component has been measured and the transverse structure functions are measured starting from the discrete data as:

$$S_{\perp}^{p}\left(\Delta y\right) = \sum_{n=0}^{N} |u_{n+j} - u_n|^p \tag{2.50}$$

All these choices are equally possible. We decided to focus on the transverse unit vector built from the longitudinal separation vector that always belongs to the (x, y) plane. Being $\mathbf{r} = (r_x, r_y, r_z)$ we define:

$$\mathbf{t} = \frac{(-r_y, r_x, 0)}{\sqrt{r_x^2 + r_y^2}} \tag{2.51}$$

From our point of view, this choice is convenient for two different technical reasons. Firstly, we need to measure the transverse velocity differences of the edges of fibers, that are by definition coherent for the whole time. To increase the quality of the measures, a Gaussian time filter will be applied on the velocity difference signal. Therefore, we need to have a signal that is time-continuous. Secondly, as it will be explained forward, the error on the experimental Lagrangian tracking procedure of the fibers is different considering different direction: therefore to chose a particular plane can be useful to reduce the tracking error.

It is known that the third order moment of the transverse velocity increments vanishes, e.g. that the pdf of the longitudinal and transverse velocity increments have a different nature [23] [24]. Notwithstanding, the even moments show a scaling behaviour similar to the longitudinal structure functions. Indeed, under the assumption of isotropy, it holds [20, Ch. 6] [24]:

$$S_2^{\perp} = S_2^{\parallel} + \frac{r}{2}\frac{\partial S_2^{\parallel}}{\partial r} \tag{2.52}$$

We do not have a theoretical based expression for $S_2^{\parallel}$; nevertheless, within the inertial range it holds the equation (2.45), therefore:

$$S_2^{\perp} = \frac{4}{3} C_2 \epsilon^{2/3} r^{2/3} \tag{2.53}$$

In isotropic turbulence it has to be expected to observe $S_2^{\parallel}/S_2^{\perp} \simeq 3/4$.

Moreover, the second order transverse structure function scaling behaviour is observable in a huge variety of experiments or numerical simulations [24] [21] [25] [26] [22] [27].

Chapter 3

Fibers flapping in turbulence

The problem of fibers characterized by a length within the inertial range flapping in a turbulent flow is formalized. Thereafter, a phenomenological theory and numerical evidences related to the dynamics of flexible fibers are presented. Finally, an original conjecture related to rigid fibers behaviour and their tumbling time is presented. The shown results are related to [17] and [16].

3.1 Coupling the motion of the fibers and the fluid

Firstly we present the model for coupling the fiber dynamics and the fluid flow. We assume that the fluid flow is governed by the incompressible Navier-Stokes equations, that are the momentum conservation (2.1) and the continuity equation (2.2) that we rewrite for convenience:

$$\frac{\partial \mathbf{u}}{\partial t} + \mathbf{u} \cdot \nabla \mathbf{u} = -\frac{1}{\rho_0} \nabla p + \nu \Delta \mathbf{u} + \mathbf{f} \tag{3.1}$$

$$\nabla \cdot \mathbf{u} = 0 \tag{3.2}$$

where $\mathbf{f}$ is the Eulerian fluid structure interaction force, i.e. for per unit volume that the fiber exerts on the fluid. The fiber position is governed by the unsteady Euler-Bernoulli 1-D beam equation [28, Ch.5, Sec. 5.2.2]:

$$\rho_l \frac{\partial^2 \mathbf{X}}{\partial t^2} = \frac{\partial}{\partial x_s} \left(T \frac{\partial \mathbf{X}}{\partial x_s} \right) - \gamma \frac{\partial^4 \mathbf{X}}{\partial x_s^4} + \mathbf{F} \tag{3.3}$$

where ρ_l is the linear density of the fiber, γ is its bending rigidity and T is the tension needed to enforce the fiber inextensibility. $\mathbf{F}$ is the Lagrangian fluid-structure interaction force, i.e. a force per unit length that the fluid exerts on the fiber.

The Euler-Bernoulli 1-D equation holds since the constituent material of the fiber is elastic and the ratio between its diameter and its length, is much smaller than unity. The (3.3) can be derived imposing the second Newton's law on an infinitesimal element of beam and substituting the elastic constitutive model to relate stress and strains. The fist term represents the inertia of an infinitesimal element, the second is the inextensibility term and the third term is related to the angular momentum equilibrium. The following constrain is needed to guarantee the inextensibility of the fiber:

$$\frac{\partial \mathbf{X}}{\partial x_s} \cdot \frac{\partial \mathbf{X}}{\partial x_s} = 0 \tag{3.4}$$

The fluid and the fiber motion are coupled at their interface by the no-slip condition:

$$\frac{\partial \mathbf{X}}{\partial t} = \mathbf{U}\left(\mathbf{X}\left(s,t\right),t\right) \tag{3.5}$$

where $\mathbf{U}$ is the fluid velocity at the position of the fiber, therefore:

$$\mathbf{U}\left(\mathbf{X}\left(s,t\right),t\right)=\int\mathbf{u}\left(\mathbf{x},t\right)\delta\left(\mathbf{x}-\mathbf{X}\left(s,t\right)\right)d^{3}\mathbf{x} \tag{3.6}$$

The the Eulerian and Lagrangian fluid-structure interaction forces are related by:

$$\mathbf{f}\left(\mathbf{x},t\right)=\int_{s}\mathbf{F}\left(s,t\right)\delta\left(\mathbf{x}-\mathbf{X}\left(s,t\right)\right)ds \tag{3.7}$$

Since we are considering a fiber freely flapping in turbulence, free-end boundary conditions are used at $s=0$ and $s=c$, c being the length of the fiber.

3.2 Flexible fibers: phenomenological theory and numerical evidences

A phenomenological theory related to flexible fibers flapping in turbulence is presented; it had been firstly developed in [17]. To describe the fluid-structure interaction, we assume a simplified viscous coupling of the form:

$$\mathbf{F}=-\mu\left(\frac{\partial\mathbf{X}}{\partial t}-\mathbf{u}\right) \tag{3.8}$$

We do not consider an anisotropic expression for the drag since the turbulent flow can be considered isotropic in a range of scale where $r\ll L$ and therefore, there are no preferential alignment. Substituting this coupling, the fiber equation holds:

$$\rho_{l}\frac{\partial^{2}\mathbf{X}}{\partial t^{2}}=\frac{\partial}{\partial x_{s}}\left(T\frac{\partial\mathbf{X}}{\partial x_{s}}\right)-\gamma\frac{\partial^{4}\mathbf{X}}{\partial x_{s}^{4}}-\mu\left(\frac{\partial\mathbf{X}}{\partial t}-\mathbf{u}\right) \tag{3.9}$$

From this equation we carry out an order of magnitude analysis; let us consider the following scales:

$$O\left(\rho_{1}\frac{\partial^{2}\mathbf{X}}{\partial t^{2}}\right)=\frac{\rho_{l}\cdot c}{\tau^{2}} \tag{3.10}$$

$$O\left(\frac{\partial}{\partial x_{s}}\left(T\frac{\partial\mathbf{X}}{\partial x_{s}}\right)\right)=\frac{T}{c} \tag{3.11}$$

$$O\left(\gamma\frac{\partial^{4}\mathbf{X}}{\partial x_{s}^{4}}\right)=\frac{\gamma}{c^{3}} \tag{3.12}$$

$$O\left(\mu\left(\frac{\partial\mathbf{X}}{\partial t}-\mathbf{u}\right)\right)=\frac{\mu\cdot c}{\tau} \tag{3.13}$$

Two characteristics time-scales can be identified from the fiber equation. Balancing fiber inertia with viscous damping, the characteristic viscous time is obtained:

$$\tau_{\mu}=\frac{2\rho_{1}}{\mu} \tag{3.14}$$

and balancing fiber inertia with bending rigidity, the characteristic elastic time is obtained:

$$\tau_{\gamma}=\alpha\left(\frac{\rho_{1}c^{4}}{\gamma}\right)^{1/2} \tag{3.15}$$

where $\alpha = \pi/22.4$ is a coefficient that depends on the fist mode of oscillation of the fiber. The ratio between the elastic and the viscous time is called damping ratio:

$$\zeta = \frac{\tau_\gamma}{\tau_\mu} = \frac{\alpha c^2 \mu}{2\rho_1^{1/2}\gamma^{1/2}} \tag{3.16}$$

As a matter of principle, the value of the dumping ratio it gives information on which kind of dynamics affects mostly the fiber motion. As a simple $1 - DOF$ viscoelastic oscillator, if the dumping ratio is $\zeta < 1$, the system is called under-dumped and the elasticity strongly affects the fiber dynamics: this means that, in still water, we expect to observe harmonic oscillation of the end to end distance of the fiber that reduces their amplitude exponentially in time. On the contrary, if $\zeta > 1$, the system is over-dumped and elastic effects are strongly inhibited. Harmonic oscillations compleately disappears and the exponential time decay is dominant.

As shown in Chapter 2, the characteristic time scale of an eddy is that is called eddy's tumbling time, and can be phenomenologically derived from Kolmogorov theory in the case of isotropic, homogeneous and stationary turbulence. We rewrite its expression (2.35) for convenience:

$$\tau(r) \sim r^{2/3}\epsilon^{-1/3} \tag{3.17}$$

By comparing the time-scales of the fiber and the characteristic time-scale of the eddies (i.e. equations (3.14), (3.15) and (2.35)), it is possible to distinguish four different regimes. For all these regimes, different flapping behaviour are expected.

under-dumped regime For $0 < \zeta < 1$ (under-damped regime), we expect that the fiber response shows an oscillatory behaviour. Therefore, we impose a resonance condition between the elastic time and the hydrodynamic one, from which a critical value of the bending rigidity can be found:

$$\tau_\gamma = \tau c \rightarrow \gamma_{crit}^{ud} \sim c^{8/3}\epsilon^{2/3}\rho_l\alpha^2 \tag{3.18}$$

Looking at the expression above, a further distinction can be made. In the limit of vanishing γ (sub-critical case), the fiber can be thought to be slaved to the flow due to the relatively faster forcing compared with its response, therefore flapping at the eddy frequency. In the opposite supercritical case, where the elastic time is much smaller than the hydrodynamic one, the fiber reaction is expected to be far more rapid than the fluid forcing. Physically, this means that the fiber flapping behaviour is mostly dominated by its own constitutive characteristics and not from the fluid forcing, e.g. it oscillates with its natural frequency.

over-dumped regime We now turn our attention to the case where $\zeta > 1$ (over-damped regime), where viscous dissipations becomes dominant. Imposing a resonance condition between the eddy turnover time and the characteristic viscous time of the fiber, a critical value of the bending rigidity can be derived:

$$\tau_\mu = \tau c \rightarrow \gamma_{crit}^{od} \sim \mu c^{10/3}\epsilon^{1/3} \tag{3.19}$$

We shall discuss the expected behaviour in the two limits also here. For $\gamma/\gamma_{crit}^{od} < 1$, the relaxation is slower than the fluid forcing and thus the fiber is slaved to the turbulence. In the opposite case the fiber is appreciably deformed only by large strains, similarly to the under-damped regime. However, in this case, elastic oscillations are not possible, and the dominant frequency is anyway expected to be the turbulence one. The fiber motion in the over-damped regime is therefore always expected to be slaved to turbulence, independently of $\gamma/\gamma_{crit}^{od}$.

under-dumped $\zeta < 1$		over-dumped $\zeta > 1$	
sub-critical $\frac{\tau(c)}{\tau_\gamma} < 1, \gamma < \gamma_{crit}^{ud}$	over-critical $\frac{\tau(c)}{\tau_\gamma} > 1, \gamma > \gamma_{crit}^{ud}$	sub-critical $\frac{\tau(c)}{\tau_\mu} < 1, \gamma < \gamma_{crit}^{od}$	over-critical $\frac{\tau(c)}{\tau_\mu} > 1, \gamma > \gamma_{crit}^{od}$
slaved	not slaved	slaved	slaved

TABLE 3.1: Flapping regimes

In three cases out of four the elastic fiber motion is expected to be slaved to the turbulence forces. This means that the fiber end to end distance oscillates at the same frequency of the turbulent eddies at its length, e.g. should shows a peak at the same frequency of turbulence at the length scale of the fiber. Formally, if f_{peak} is the peak frequency of the end to end distance and $f_{turb} = \frac{1}{\tau(c)}$ is the turbulence frequency at the length scale of the fiber, it shall results:

$$\frac{f_{peak}}{f_{turb}} \simeq 1 \tag{3.20}$$

This behaviour had been shown by direct numerical simulations (DNS) fully resolving the fluid-structure coupled problem stated above [17] [16].

For those regimes fully slaved to the flow, the fiber may be viewed as a Lagrangian tracker of turbulent eddies, exploitable for evaluating not only their characteristic time but also two-point statistical quantities such as, e.g., scaling exponents of velocity structure functions. In other words, the probability density function of longitudinal velocity differences at the fiber length can be measured as the velocity differences of the extremes of the fibers. If the fiber is rigid, e.g. the under-dumped and over-critical regime, it oscillates at its own natural frequency. If the fiber is perfectly rigid, the end to end distance will not change in time.

The adopted numerical method to couple the problem is called Immersed Boundary Method (IBM) [29]; by using this method, the numerical grid does not need to conform to the geometry of the object. Indeed, the object is replaced by the Lagrangian force force density distribution **F** which mimics the presence of the body in the fluid and restores the velocity boundary conditions on the immersed surfaces. Therefore, even if it can be considerate accurate, it does not guarantee a completely realistic coupling between the fluid and the structure motion. Another assumption lies in the Euler-Bernoulli beam equation: it does not represent the motion of an elongated 3-D object, but it approximates it to a 1-D geometry. Formally, it holds in the limit of vanishing aspect ratio. For both these reasons, to do physical experiments tracking the position of flexible fibers can still be worthy.

3.3 Rigid fibers: an original conjecture

The problem of a rigid fibers spinning in turbulence has not been investigated already. Our conjecture consists in the fact that rigid fibers can be used to measure transverse velocity increments at the scale of the fiber length. In other words the assumption consists in thinking that a rigid fiber swimming in a turbulence flow, spins at the same frequency of the eddies of its length scale. This can be seen measuring its tumbling time. The tumbling time is a characteristic time-scale that can be seen as the main frequency at which a rigid body spins:

$$\tau_{tamb} = \left(\frac{d\hat{\mathbf{r}}}{dt} \cdot \frac{d\hat{\mathbf{r}}}{dt}\right)^{-1/2} \tag{3.21}$$

The orientation unit vector is defined as:

$$\hat{\mathbf{r}} = \frac{\mathbf{r}}{|\mathbf{r}|} \tag{3.22}$$

An expression to evaluate the tumbling time an eddy directly from the Lagrangian velocity differences (i.e. the velocity differences between two particles freely mooving in a turbulent flow) can be derived thinking about the instantaneous variation of the orientation unit vector, defined in (3.22). The time derivative of the length of the separation between two particles can be carried out as:

$$\frac{d|\mathbf{r}|}{dt} = \frac{\mathbf{r} \cdot \delta\mathbf{u}}{|\mathbf{r}|} \tag{3.23}$$

By applying the chain rule, the time derivative of the unit orientation vector can be evaluated as:

$$\frac{d}{dt}\left(\frac{\mathbf{r}}{|\mathbf{r}|}\right) = \frac{\delta\mathbf{u}}{|\mathbf{r}|} - \mathbf{r}\frac{\mathbf{r} \cdot \delta\mathbf{u}}{|\mathbf{r}|^3} \tag{3.24}$$

An expression for the tumbling time that depends on the velocity differences and on the length of the separation vector can be therefore derived:

$$\tau_{tambl} = \left(\frac{|\delta\mathbf{u}|^2}{|\mathbf{r}|^2} - \frac{(\delta\mathbf{u} \cdot \mathbf{r})^2}{|\mathbf{r}|^4}\right)^{-1/2} \tag{3.25}$$

If we define respectively the longitudinal velocity differences vector and the transverse velocity difference vector as:

$$\delta\mathbf{u}^{\parallel} = \delta u^{\parallel}\frac{\mathbf{r}}{|\mathbf{r}|} = \left(\frac{\delta\mathbf{u} \cdot \mathbf{r}}{|\mathbf{r}|}\right)\frac{\mathbf{r}}{|\mathbf{r}|} \tag{3.26}$$

$$\delta\mathbf{u}^{\perp} = \delta\mathbf{u} - \delta\mathbf{u}^{\parallel} \tag{3.27}$$

we can write that:

$$\delta\mathbf{u} = \delta\mathbf{u}^{\parallel} + \delta\mathbf{u}^{\perp} \tag{3.28}$$

The longitudinal velocity differences are negligible if we consider the extremes of an almost rigid fiber, therefore:

$$\delta\mathbf{u} \simeq \delta\mathbf{u}^{\perp} \tag{3.29}$$

$$\tau_{tabl,rigid} = \frac{|\mathbf{r}|}{|\delta\mathbf{u}|} \tag{3.30}$$

Two significant questions arise comparing (2.35), (3.30), and (3.25).

What does rigid mean? Considering equation (3.25) and (3.25) we can say that the fiber is rigid compared to the fluid forcing since:

$$\frac{\tau_{tambl,rigid}}{\tau_{tambl}} \sim 1 \tag{3.31}$$

Physically, this means that the longitudinal velocity differences does not affect significantly the tumbling time of the fiber.

How does a rigid fiber spin in a turbulent flow? We suppose that the tumbling time of a fiber characterized by a length c within the inertial range swimming in a turbulent flow spins at the same frequency of the eddies at its length scale; in other worlds:

$$\tau_{tamb,rigid}\left(c\right) \sim c^{2/3}\epsilon^{-1/3} \tag{3.32}$$

If this is the case, we suppose that to measure transverse velocity increments by tracking the edges of the fiber is possible. If this happens and, possibly, under which condition, has not been investigated already; which are the parameters that govern this phenomenon is an open question. Both this questions are subject of the present work.

Despite the fact that to measure the transverse velocity increments is less useful than longitudinal velocity differences from a turbulence modelling point of view, a methodology to measure the eddies tumbling time at a fixed scale can be useful; indeed, the eddies tumbling time can be difficult to measure directly with Lagrangian tracker also if long measures are available.

3.4 Stokes numbers

The Stokes number is a non-dimensional group defined as the ratio of a characteristic time of an object (usually a particle, e.g. 0-D object) to a characteristic time of the flow.

$$Stk = \frac{\tau_{obj}}{\tau_{flow}} \tag{3.33}$$

τ_{obj} is usually an exponential time decay; a quantity Q is subjected to exponential decay if it decreases at a rate proportional to its current value, that is:

$$Q\left(t\right) = Q_0 e^{-\lambda t} \tag{3.34}$$

where Q_0 is its initial value. λ is called exponential time decay. This value can be derived in many different scenarios, i.e. considering different phenomena. For instance, if we consider a particle heavier that the fluid released into it, it will reach a steady settle velocity because of the drag force: the exponential decay is a measure of how long does it takes to reach the final settling velocity.

For a slender body in a Stokesian flow, conventionally, two characteristic time scale are defined: the translational and the rotational relaxation time. The first one is conceptually similar to the particle's one: it can be measured by dragging a fiber up to a constant velocity and than releasing it in still water; the fiber will decelerate because of the drag force and stop after a while. By measuring its decaying velocity and then interpolating it with an exponential function, it is possible to measure the translational relaxation time. Considering the rotational case, the procedure is similar but an initial value of angular velocity has to be imposed; thereafter, the angular velocity decay can be measured and the same procedure has to be followed.

Since to measure experimentally the Stokes number of a fiber is not feasible, two different possibilities can be considered:

- perform some direct numerical simulation with which it is possible to impose the initial condition on the fiber velocity without modify the initial fluid flow;
- consider the slander body theory, even though it is related to body with a length scale smaller that the Kolmogorov microscales [28, Ch.2, Sec. 8], i.e. a length scale for which the viscous term is more important than the non-linear term.

We will consider a value for the Stokes number evaluated theoretically through the slender body theory, so for a fiber characterized by $c < \eta$; therefore, this analysis is not correct. The Stokes number can be evalueted as [30]:

$$Stk = \frac{1}{32}\frac{\rho_v}{\rho_w} Re_d \cdot a \cdot ln\left(a^2 \cdot e\right) \tag{3.35}$$

where:

$$a = \frac{d}{c} \tag{3.36}$$

and

$$Re_d = \frac{U \cdot d}{\nu} \tag{3.37}$$

are the aspect ratio and the diameter Reynolds number respectively. Even thought the fact that this analysis is affected by an intrinsic error, this formula will be considered as a proxy of the fiber real behaviour. Figure 3.1 shows how the Stokes numbers depends on the Reynolds number of the fiber diameter and on its aspect ratio. From this formula, some important consideration can be derived:

- the higher is the turbulence intensity (so the diameter Reynolds number), the higher is the Stokes number; this fact holds because of the (3.33), a priori of the Stokesian flow assumption. Indeed, $Stk = \frac{\tau_{obj}}{\tau_{flow}} = \frac{\tau_{obj} \cdot u_{rms}}{d}$; moreover, this fact physically sounds: the higher is the turbulence intensity, the faster is the fluid flow around the fiber and the harder will be for the it to follow the fluid flow;
- the smaller is the aspect ratio, the smaller is the Stokes number; this consideration is not ensured also out of the micro-scales.

A direct evaluation of the Stoke's number for fibers characterized by a length within the inertial range is being carried out by Prof. Andrea Mazzino and Edoardo Rosti[1] (not yet published) by means of DNS.

In order to consider the added mass effect, instead of using ρ_l as the linear density, a new linear density can be used, defined as follow:

$$\rho_{l,new} = \rho_l + \rho_w \frac{\pi d^2}{4} = \frac{\pi d^2}{4}\left(\rho_v + \rho_w\right) \simeq \rho_w \frac{\pi d^2}{2} \tag{3.38}$$

Therefore, a modified expression for the fiber's volume density can be considered:

$$\rho_{v,new} \simeq 2 \cdot \rho_w \tag{3.39}$$

Taking it to account this effect likely increases the Stokes number.

[1] post-doc at KTH Royal Institute of Technology

An important comment From what said above, it seems that the lower is the turbulence intensity the better will the fiber follow the turbulence flow; and this is true. Nevertheless, if the aim is to have a flexible fiber that is slaved to turbulence, the higher is the turbulence intensity, the easier will be for the fluid force to bend it, so to fall in one of the slaved regimes. This fact can leads to a conflict in searching an optimal configuration to test the flexible fiber case.

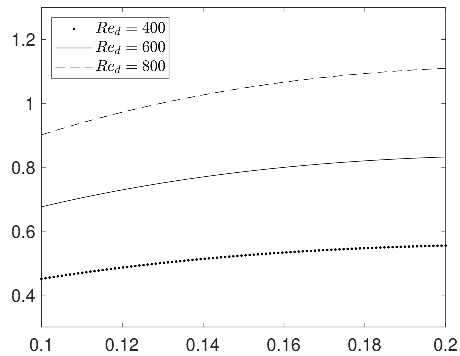

FIGURE 3.1: Stokes number depends on the aspect ratio $a = d/c$ and on the fiber Reynolds number $Re_d = U \cdot d/\nu$.

3.5 From theory to polymeric fibers hand-crafting

In order to hand-craft polymeric fibers with suitable features, three different properties have to be controlled: firstly, **mass properties**, because the neutral buoyancy of fibers is required; the fibers are required to be almost neutral respect to the buoyancy force; secondly, **optical property**, because the extremes of the fibers must be traceable under laser light; finally **mechanical properties**, since the fiber flexibility has to be controlled; ideed, different bending rigidity must be tried. To respect all these constrains, the fibers are hand-crafted by means of polydimethylsiloxane (PDMS) and rhodaminea and a new casting technique is developed. Some observation about they mass and the mechanical properties are discussed below.

We use Polydimethylsiloxane (PDMS) to hand-craft the fibers. In fact, this material has all the required properties: firstly is possible to easily hand craft PDMS samples. Afterward, PDMS is naturally transparent, and it is possible to dye it while hand-crafting: as shown in Chapter 5, these two features are indispensable in the Lagrangian tracking procedure. Finally, as shown below, it has suitable volume density: since we need to produce a neutrally buoyant fiber, PDMS density is $\sim 965\ [kgm^{-3}]$.

We do further manipulation of the theory derived in Section 3.2 in order to understand which mechanical and geometrical properties we require from the fibers to be flexible or rigid. Due to the fact that both the damping ratio and the critical banding rigidity depend on the fiber's characteristics (c and γ), we have that the flapping regime depends on both the fiber and the turbulence characteristics.

Before producing the fibers, it can be advisable to assume a reasonable constitutive model for the polymer (possibly linear elastic) and to collect informations about the constituent parameters. Than, we have to know the turbulence properties in our set up (old experiments) such that them can be reproduced in lab. This will help us in estimating the critical values for the dumping ratio and the bending rigidity (ζ and γ_c).

Assuming that the turbulence properties and the mechanical properties of the material can not be changed much, we can only tune the geometrical properties of the fiber in order to have it flapping in a desirable regime. Therefore, it can be useful to show how d and c affect the dumping ratio and the critical bending rigidity explicitly. Moreover, since we have to fix some values of the fiber's length c within the inertial range, we want to show how these parameters are affected by the fiber's diameter for different values of c.

If we considerer a fiber characterized by a circular cross-section we have that its linear density is:

$$\rho_l = \rho_v \, \frac{\pi \, d^2}{4} \tag{3.40}$$

Assuming an homogeneous and isotropic constitutive low for the hydro-gel and that its length is at least ten times its diameter (Euler-Bernoulli beam) we can express the banding rigidity as:

$$\gamma = E \, J \tag{3.41}$$

where $J = \frac{\pi \, d^4}{64}$ is the second order moment of the circular cross section. The damping ratio can be written as:

$$\zeta = \frac{\tau_\gamma}{\tau_\mu} = \frac{\alpha c^2 \mu}{2 \rho_f^{1/2} \gamma^{1/2}} = \left(\frac{8 \alpha \nu \rho_w}{\pi E^{1/2} \rho_v^{1/2}} \right) \frac{c^2}{d^3} \tag{3.42}$$

For each value of c, the critical value d_c over which we are under-dumped (elasticity is governing the motion) and vice versa, is found by requiring that $\zeta = 1$, so we have:

$$d_c = \left(\frac{8 \alpha \nu \rho_w}{\pi E^{1/2} \rho_v^{1/2}} \right)^{1/3} c^{2/3} \tag{3.43}$$

In the under-dumped regime ($d > d_c$) we have that:

$$\gamma_c^{ud} = c^{8/3} \epsilon^{2/3} \rho_l \alpha^2 \tag{3.44}$$

from which we can easily provide and expression for the critical value of the fiber diameter in the under-dumped case, therefore:

$$d_c^{ud} = \left(4 \alpha \epsilon^{1/3} \rho_v^{1/2} E^{-1/2} \right) c^{4/3} \tag{3.45}$$

In the over-dumped regime ($d < d_c$) we have that:

$$\gamma_c^{ud} = \mu c^{10/3} \epsilon^{1/3} \tag{3.46}$$

from which we can evaluate an expression for the critical value of the fiber's diameter in the under-dumped case, therefore:

$$d_c^{od} = \left(\frac{64 \nu \rho_w \epsilon^{1/3}}{\pi E} \right)^{1/4} c^{5/6} \tag{3.47}$$

Fixing some realistic range of values for the Young's modulus, it is possible to see which regimes we can actually investigate with feasible diameter.

Assuming the values shown in Table 3.2, we can calculate the critical values of the diameter. As shown in Figure 3.2, the thinner is the fiber, the easier it to fall in the under-dumped regime and the easier is to show the longitudinal turbulence statistics; the higher are the dissipations, the easier the turbulence is to investigate. Moreover, we assumed to have an Euler-Bernoulli beam so that the diameter of the cross-section must be at most $1/10$ of the fiber's length to have negligible shear strain, but this is never a problem.

To investigate the rigid case, we need to produce a fiber that both over-dumped and in the over-critical case. To ensure this, the turbulence intensity can be reduced, and the diameter has to be increased up to $1\,mm$. To maintain the Euler-Bernoulli hypothesis can become a problem, but it is no more necessary from a stress-strain point of view. It can become an issue from the Stokes number prospective.

However, this analysis strongly depends on the value of the Young's modulus and of the dissipations: for this reason it is important to have a good a priori estimation of the mechanical properties of the PDMS and of the turbulence intensity.

ρ_w $[Kg\,m^{-3}]$	ν $[m2\,s^{-1}]$	ρ_v $[Kg\,m^{-3}]$	E $[N\,m^{-2}]$	ϵ $[m2\,s^{-3}]$	α $[-]$
999.84	$1.004 \cdot 10^{-6}$	1000	1000	10^{-3}	$\pi/22.4$
999.84	$1.004 \cdot 10^{-6}$	1000	1000	10^{-4}	$\pi/22.4$
999.84	$1.004 \cdot 10^{-6}$	1000	100	10^{-3}	$\pi/22.4$
999.84	$1.004 \cdot 10^{-6}$	1000	100	10^{-4}	$\pi/22.4$

TABLE 3.2: Representative values of the fluid, turbulence and material characteristics; the order of magnitude of the dissipation is achievable in our lab set-up and the Young's modulus is from [1]

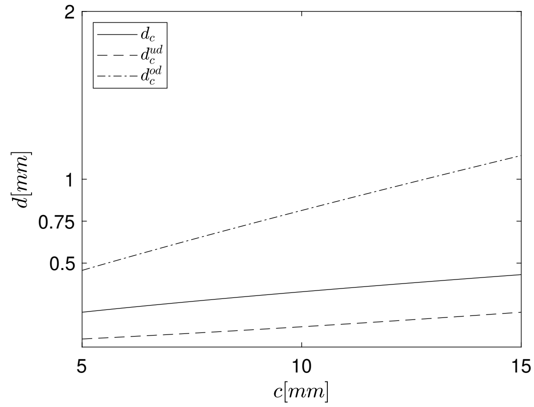

(a) $E = 1000kPa, \epsilon = 10^{-3}m^2s^{-3}$

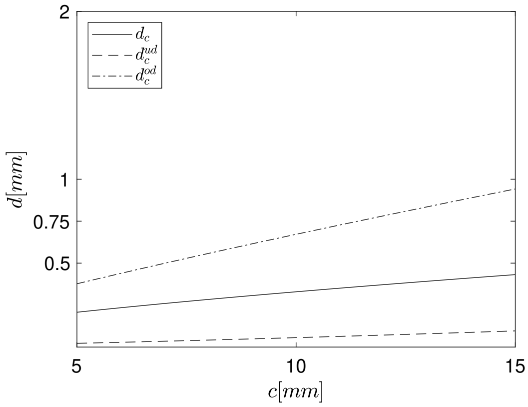

(b) $E = 1000kPa, \epsilon = 10^{-4}m^2s^{-3}$

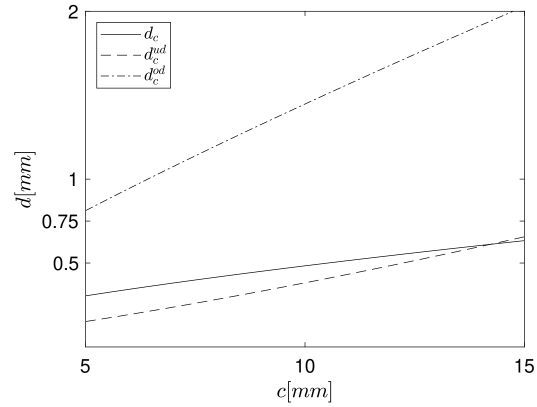

(c) $E = 100kPa, \epsilon = 10^{-3}m^2s^{-3}$

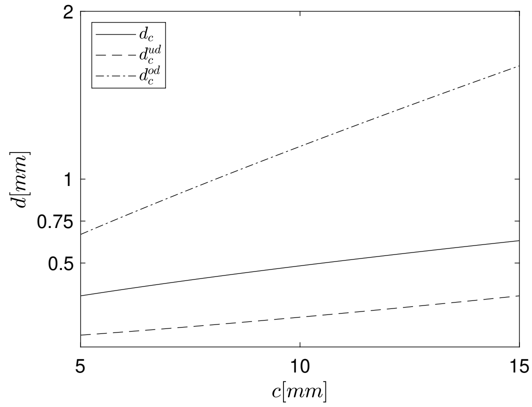

(d) $E = 100kPa, \epsilon = 10^{-4}m^2s^{-3}$

FIGURE 3.2: critical diameter for the dumping regime (d_c), critical diameter for the flapping regime in the over-dumped case (d_c^{od}), critical diameter for the flapping regime in the under-dumped case (d_c^{ud}).

Chapter 4

An overview of photogrammetry

A brief overview of the theory and experimental methods related to photogrammetry techniques is presented. Firstly the theoretical foundations of particle pothogrammetry are explained; thereafter, the needed experimental instrumentation is described and some issues related to this aspect are discussed.

4.1 Theory of photogrammetry

Photogrammetry is a technique that consists in taking two or more pictures of the same object from different points of view. If the coordinates of some points of the pictures are known a priori, it is then possible to determine the position of all the others points in the space observed by the cameras [31].

Firstly the concept of pinhole camera model has to be introduced; the pinhole camera model describes the mathematical relationship between the coordinates of a point in three-dimensional space and its projection on the image plane of an ideal pinhole camera, where the camera aperture is described as a point. For the sake of simplicity, the image plane is interposed between the focal point and the object point. The fundamental mathematical concept of particle tracking by means of photogrammetry is the so called collinearity condition that states that the object point P, the camera projective center O and the image point P' belong to the same straight line.

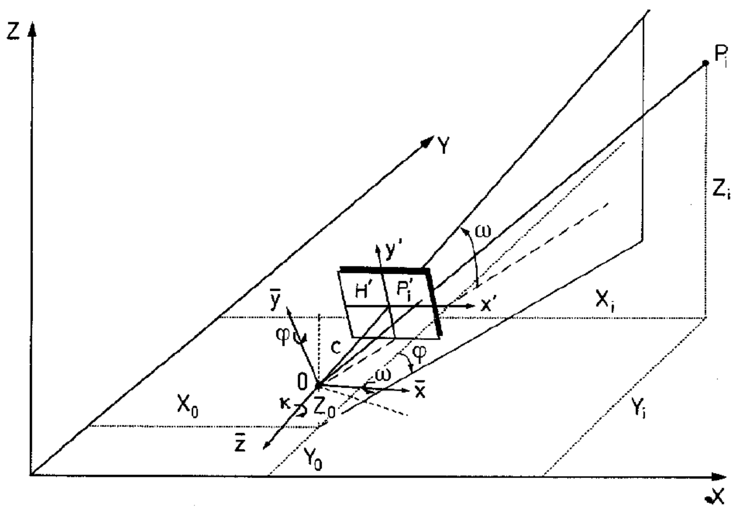

FIGURE 4.1: Collinearity condition for an inverted pinhole camera model.

This concept can be observed in Figure 4.8. Let us assume that (x, y) are the coordinates of P' in the image reference frame, (X_0, Y_0, Z_0) are the coordinates of the camera in the object reference frame, $(\omega, \varphi, \kappa)$ are the orientation angles of the camera; c is the focal length. In can be derived from geometrical consideration the two following mathematical relationship between the image coordinates and the real coordinates:

$$x'_i = x_h - c \cdot \frac{a_{11}(X_i - X_0) + a_{21}(Y_i - Y_0) + a_{31}(Z_i - Z_0)}{a_{13}(X_i - X_0) + a_{23}(Y_i - Y_0) + a_{33}(Z_i - Z_0)} \tag{4.1}$$

$$y'_i = y_h - c \cdot \frac{a_{12}(X_i - X_0) + a_{22}(Y_i - Y_0) + a_{32}(Z_i - Z_0)}{a_{13}(X_i - X_0) + a_{23}(Y_i - Y_0) + a_{33}(Z_i - Z_0)} \tag{4.2}$$

where (x_h, y_h) are the image coordinates of H' that is the camera center. Some more relations have to be carried out to considerer some other parameters. The radial symmetric length distortion and the decentering has to be considered; a mathematical model ([31, Ch. 3, Sec. 1]) involving five new parameters can be derived:

$$\overline{x'_i} = x'_i + dx_i, \ \overline{y'_i} = y'_i + dy_i \tag{4.3}$$

where:

$$dx_i = x'_i \left(k_1 r'^2 + k_2 r'^4 + k_3 r'^6 \right) + p_1 \left(r'^2 + 2x'^2_i \right) + 2p_2 x'_i y'_i \tag{4.4}$$

$$dy_i = y'_i \left(k_1 r'^2 + k_2 r'^4 + k_3 r'^6 \right) + p_1 \left(r'^2 + 2y'^2_i \right) + 2p_2 x'_i y'_i \tag{4.5}$$

Moreover, the influence of electronic effects (unknown difference of the clock rates of camera and framegrabber) can be modelled as an affine transformation:

$$\tilde{x}_i = a_0 + a_1 \overline{x'_i} + a_2 \overline{y'_i} \tag{4.6}$$

$$\tilde{y}_i = b_0 + b_1 \overline{x'_i} + b_2 \overline{y'_i} \tag{4.7}$$

All of these consideration can be summarized in the following functional relation between the camera coordinate and the real reference frame that is a generalization of the collinearity condition:

$$(x, y) = f\left(X_0, Y_0, Z_0, \omega, \varphi, \kappa, X, Y, Z, \Phi\right) \tag{4.8}$$

Φ is a vector of parameters, such as the length distortion and the focal length. It is than clear that knowing (x, y) (so taking pictures of one or more particles), (X_0, Y_0, Z_0), $(\omega, \varphi, \kappa)$ and Φ by calibration procedures, since at least this parameters are known for a couple of cameras, (X, Y, Z) can be determined solving a system of equation or by regression in case of more than two cameras. It can be seen that for more that four cameras, the accuracy will not increase significantly.

4.2 High speed recording

The main issues to deal with using photogrammetry in the context of fluid flow description are the following: in this context photogrammetry is used to track objects that move in time, so it is necessary to sampling images at a frequency high enough to capture correctly particles motion. Indeed, if the sampling frequency is not high enough, mismatch between particles tracked in two subsequent time step are possible. For this reason the need of high speed cameras rises. High speed cameras are cameras that are able to capture image sequences at an high frame rate.

Two different criterion can be used to understand which is the minimum frame-rate that allows a correct particle tracking:

- an empirical criterion, for which short time videos are recorded; by means of a qualitative observation of two subsequent frames, it is possible to understand if the time-step is small enough to allow a correct distinction between particles; in other words, the particles motion has to be "smooth enough";
- a theoretical criterion that consists in considering the highest frequency of a turbulent flow in a Kolmogorov sense. If we want to look at the whole inertial range (between L and η), it is necessary to sample at least at the smallest eddies turbulence frequency that is from Kolmogorov theory:

$$f_\eta = \left(\frac{\epsilon}{\nu}\right)^{1/2} \tag{4.9}$$

  This sampling frequency is not sufficient if a mean flow is present, so that a further increase of the frame rate has to be taken in to account. It can be considered to be proportional to $\Delta f \sim max(U)/L$ where $max(U)$ is the maximum intensity of the mean flow.

4.3 Lighting

The necessity of high speed recording leads to a second issue: the higher the frame-rate is, the less light is captured by the cameras; for this reason in the context of high speed recording, high power lightning such as laser light is also needed. The laser light is used during the recording procedure, but during the calibration procedure a led light is used. Moreover, by using laser light, it is possible to control the light wavelength, and to use a very small part of the light spectrum: this fact helps while using fluorescent material as traces and optical filters that cut certain wavelengths.

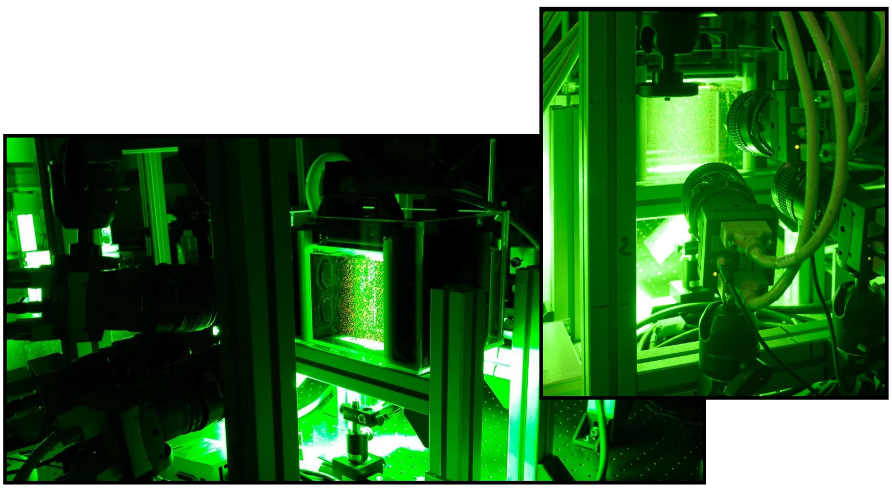

FIGURE 4.2: A picture of the set-up illuminated by the laser light at full power, kindly provided by F.G. Michalec.

Chapter 5

Methods

In the current Chapter, the set-up used to generate turbulence, the fiber hand-crafting protocol and the methodologies for measuring the flow field and for tracking the fiber position are described. Finally, the protocols to carry out two different type of experiments are presented.

5.1 Experimental set-up

The experimental set-up is mounted on a table of almost $5\,m^2$ (Figure 5.1). The set-up consists in an aquarium with a turbulence generator, held up by a structure of metal beams. The aquarium is illuminated with a laser beam from below and then reflected down again by a mirror placed on the aquarium ceiling. The laser light is squared shaped by means of two optical lenses: the first one is a convex lens that reduces the laser beam to a small point; the second expands it again in a squared shape.

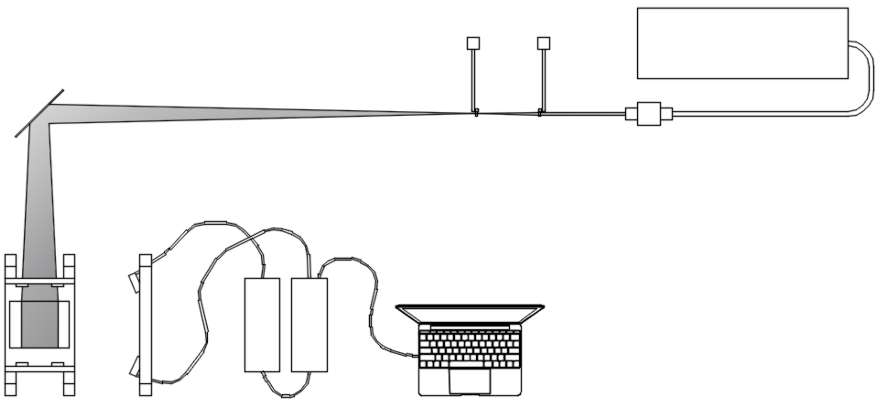

(a) top view

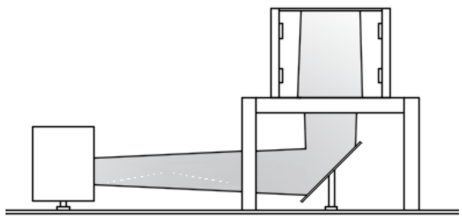

(b) front view

FIGURE 5.1: Sketch of the table of the experimental set-up.

As shown in Figure 5.1(a), the aquarium is placed at such a distance that the size of the beam illuminates precisely the observation volume. Since the table is not large enough, a mirror is placed with a 45^o inclination on the table corner to extend the light path. The camera system consists in four cameras focused stereoscopically on the observation volume: the cameras are connected to two fast writeable hard disks that are connected to a laptop.

The aquarium is equipped with a turbulence generator (Figure 5.1(b)): the forced flow domain is a rectangular box of $120 \cdot 120 \cdot 140\,mm^3$. The flow is forced mechanically from two sides by two sets of four counter-rotating disks (Figure 5.2). The disks have artificial roughness elements and are driven by a closed loop controlled servo motor. The motor is installed on top of the forcing unit and drives the counter-rotating disks through a fixed gear chain, where all disks rotate at the same rate according to the scheme shown in Figure 5.2. The actual observation volume of approximately $80 \cdot 80 \cdot 80\,mm^3$ was centred with respect to the forced flow domain, mid-way between the disks. The presented data were recorded with a disk rotational speed of $400\,rpm$.

The four high speed cameras are used at $400\,fps$, that is enough to look at velocity differences inside the whole inertial range. The cameras are shielded or not with optical filters depending whether the fibers or the particles, respectively, have to be observed. The data are stored in real time on the two fast-writeable hard disks and then transferred on traditional supports to be analysed.

The laser is used to illuminate the observation volume in full power at $34\,A$; it is necessary to use laser light since the higher the frame rate is, the less light can the cameras capture. Led lights in front of the aquarium are used to illuminate the volume during the calibration procedure: indeed, a calibration target - an object with known coordinates - is put inside the volume and than a snapshot for each camera is captured. During the calibration procedure, the frontal illumination ameliorates the cameras view of the calibration target.

With this set-up it is possible to generate a turbulent flow field that is neither homogeneous nor isotropic in the whole volume. The generated turbulent flow field is stationary in the whole volume, meaning that averaging over time on different - long enough - time windows, the mean flow is always the same. Nevertheless, the obtained flow field can be considered slightly variable under space translation, meaning that the mean flow gradients acts on a scale much greater that the integral scale.

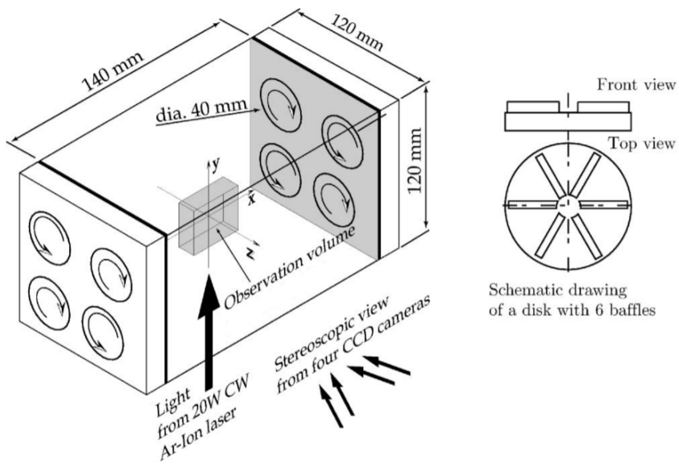

FIGURE 5.2: setup

5.2 Fibers hand-crafting

Fibers are hand-crafted with Polydimethylsiloxane (PDMS). The standard procedure to make PDMS consists in mixing an elastomer with a curing agent (ratio 10/1) by stirring the solution for at least $10\,minutes$; the prepared solution is therefore desiccated in a vacuum chamber and placed in a Petri dish: if any bubbles form while the solution is poured, a pipette can be used to burst them out. Eventually, the mixture is baked in the oven at 80^oC for at least $3\,hours$.

The idea is to produce fibers that have edges dyed with sulforhodamine b: indeed, by means of optical filters, only the dyed edges are visible under laser light. For this purpose, the following routine is carried out:

1. two different beakers of PDMS are prepared at the liquid state: one of pure PDMS and the other mixed with sulforhodamine b;

2. a first thin layer of rhodamine-dyed PDMS is poured in a Petri dish and baked in the oven for only 15 minutes, to obtain a not completely cured solution;

3. a second thicker layer of pure PDMS is added and cooked for 2 hours: at this point of the procedure, the first layer is completely cured, whereas the second is not;

4. the third rhodmine-dyed layer is added and the whole sample is cooked for at least 1 hour, to ensure its complete polymerization;

5. the sample is pierced with a special cylindrical puncher orthogonally to the layers to pull out the fibres.

In this procedure, the baking time are shortened so that the PDMS solution does not cure completely when the following layer is added. This allows the above layer to stick to the lower one without letting the sulforhodamine to diffuse in the pure PDMS layer. The reported time has been optimized in order to lower the sulforhodamine diffusion, still maintaining the stickiness of the layers.

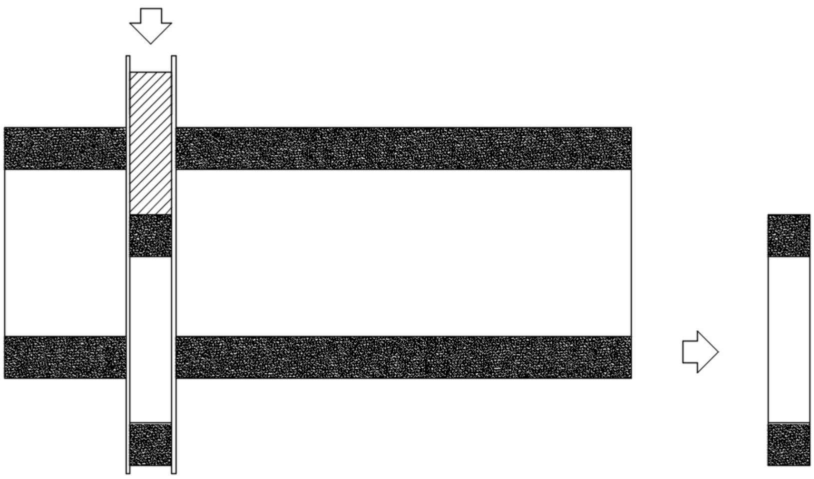

FIGURE 5.3: Punching scheme.

Three layered fibers are obtained. The diameter can be controlled changing the puncher size, and three commercial punchers are available with the following diameters: $0.50 - 0.75 - 1.00\,mm$. The fiber length can be controlled by changing the thickness of the second layer. With a single sample of about $\sim 10 \cdot 10\,mm^2$, it is possible to punch more than 200 fibers. In Figure 5.10 three fibers are shown as they are captured in a single snapshot: the optical filters make only the rhodhamine dyed edges visible, hiding the reflections of the laser light on the clean PDMS core and on the particles.

5.3 3-D Particle Tracking Velocimetry (PTV)

The methodology followed to track the particles in the flow field and to measure their Lagrangian velocity is explained. Firstly, the system has to be calibrate; afterwards, a series of images (one for each camera and for each time-step) has to be recorded; after applying a pre-processing routine useful to have clearer pictures, the images are analysed and the particles are tracked in space and linked between two subsequent time-step. Finally, a post processing routine on the rough particles coordinates is applied to calculate Lagrangian derivatives.

calibration Plainly, the calibration procedure consists in make the system understanding in which position are the cameras and how they are oriented. It consists mainly in taking four pictures of the calibration target that is a shaped object on which points of known coordinates are drown (Figure 5.4). Therefore, the four images are manually filtered in order to delete reflections and other impurities that can affect the points detection. A comparison between a cleaned calibration target picture and the original is shown in Figure 5.4: while on the 5.4(a) mismatch between the white dots and the other white stains that are present on the left side of the image are possible, on the 5.4(b) only the white dots are visible.

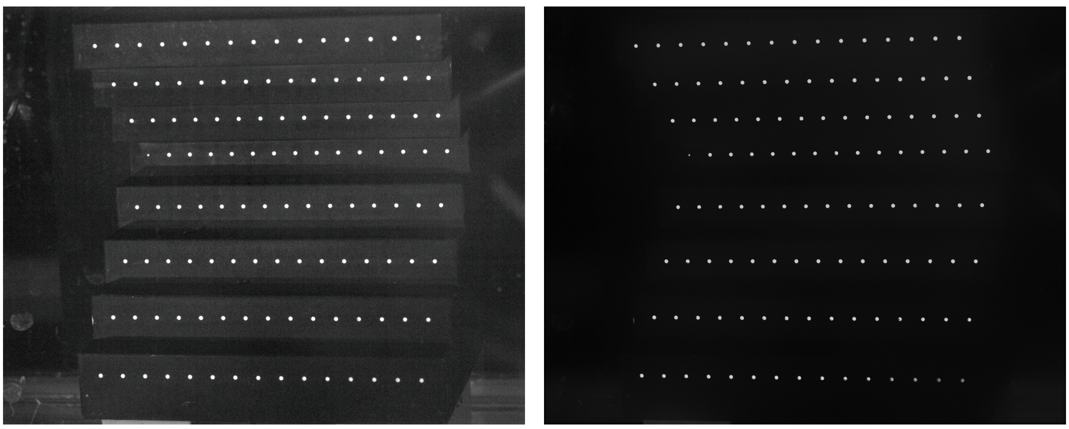

(a) first camera (b) second camera

FIGURE 5.4: The calibration images: they represent the calibration block seen from the four different cameras.

The white dots of the calibration block are detected in the 2-D image coordinates space. Therefore, the white dots coordinates are known in the image coordinate space of the four camera for a large number of points (the number of white dots). The collinearity equation (4.8) states that an under-determined relationship exist, relating the image coordinates of a point and the calibration parameters; the calibration parameters are the camera position and orientation as well as the other distortion factors discussed in Chapter 4. This functional relation can be written for all the white dots coordinates of the images in order to have an over-determined system of equations where the unknowns are the calibration parameters. The system being over-determined, a regression routine is used to fix the calibration parameters.

image pre-processing In Figure 5.5 it is shown the flow field seeded with white reflective non-fluorescent particles; an image pre processing routine is carried out in order to optimize the number of tracked particles.

1. the images are formatted as 8 bit grey-scale;
2. in order to subtract the background from the images, the time-mode of grey value of each pixel is evaluated and then subtracted from each picture; this procedure allows to remove fixed in time reflections or glass dirtying;
3. since the rough wheels that are used to generate the turbulence are still visible in the frames, the edges or the images are setted to black; moreover, also the low and the top of each picture is cut slightly, to avoid some edge effects.

The post processing routine is carried out for all the time-steps and for each camera.

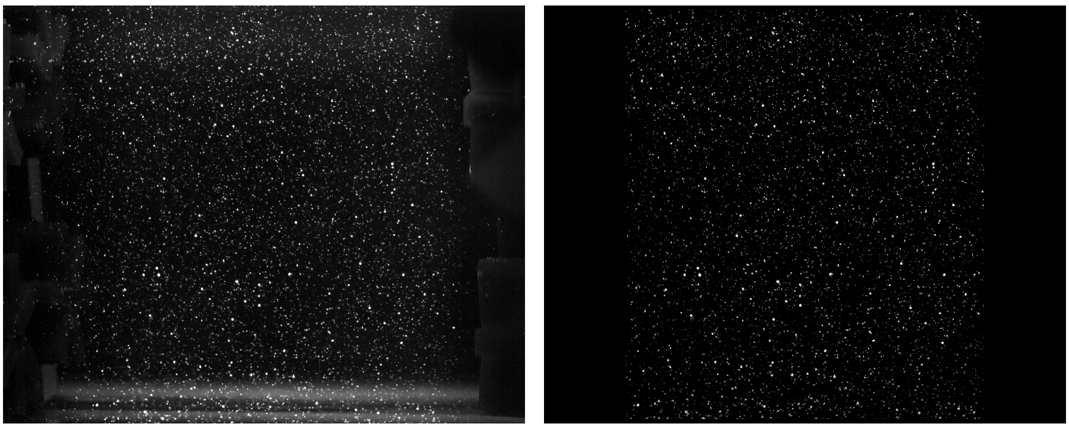

(a) original (b) after image pre-processing

FIGURE 5.5: View of the first camera without optical filter.

sequencing and tracking The sequence and tacking procedure consists in three main steps: firstly the particles position is detected by means of the images and the calibration parameters; then, the positions of each particle is linked between different time steps when it is possible. The result is a series of text files called *ptv_is.timestep*, one for each time-step. Further post processing on *ptv_is* files is necessary to evaluate Lagrangian velocities and the spatial derivatives associated to each trajectory.

The post processing routine is applied on the $ptv_is.timestep$ files that are characterized by a high noise on the particles position: this is done in order to have a reliable evaluation of the time derivatives that otherwise would leap: indeed, to take a derivative of a noised function leads easily to unstable results.

Three different kind of files are generated by this procedure:

xuap.timestep: contain both the information about the particle position as the *ptv$_i$s.timestep* files, but also the filtered position and the Lagrangian derivatives along the particle trajectories, i.e. the Lagrangian velocity and acceleration;

traj.timestep: contain the same informations of the *xuap.timestep* files, but in a different format: for each time-step, i.e. for each file, the complete trajectory of the particles firstly seen in that time-step are reported.

When producing *xuap.timestep* files along trajectories, moving cubic polynomials of 3^{rd} order are fitted to the raw particle positions. From this filtered positions, velocities, and accelerations are produced and written into *xuap.timestep* files [32]. The *traj.timestep* files contains the same information of the *xuap.timestep*, however in a different format; therefore, they are created subsequently to the *xuap.timestep* files.

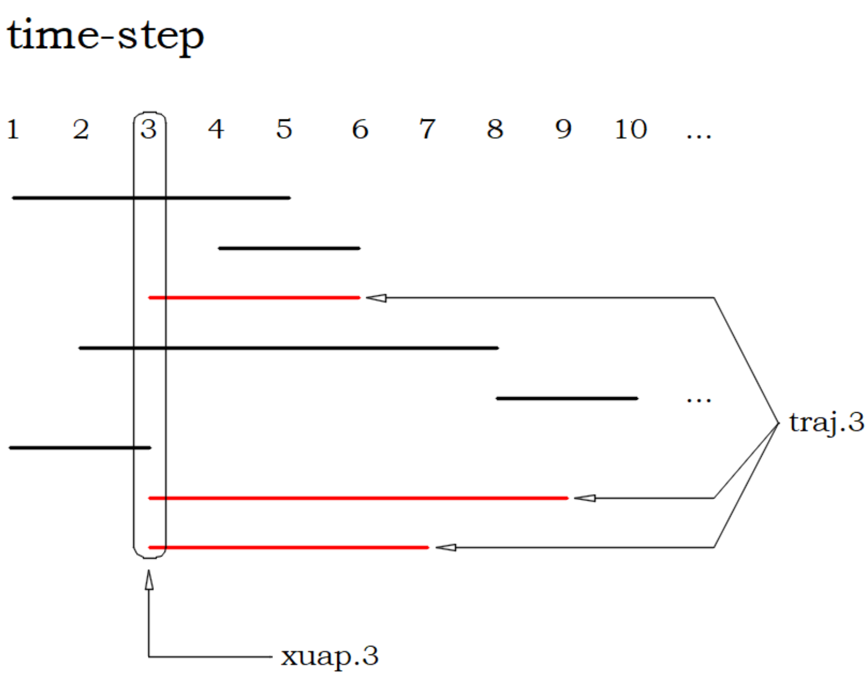

FIGURE 5.6: Representative scheme of the differences between *xuap.timestep* and *traj.timestep* file format.

flow field visualisation The 3-D flow field can be visualized with different techniques. One possibility is to show iso-surfaces of a significant scalar quantities, e.g. the enstrophy or the velocity magnitude. Otherwise, the Lapunov exponent can be used to detect barries to transport, that are surfaces through which mass can not flow [33]. Otherwise, Lagrangian Coherent Structures (LCS) or Eulerian Coherent Structures (ECS) of different nature can be detected and displayed: an example of easy to detect ECSs are the structures defined by means of the so called $Q - criterion$, that define a vortex as a region in which the $Q > 0$, where Q is the second invariant of the velocity gradient tensor [34]; LCS can be detected also from a Lagrangian point of view, for instance using the Direct Lyapunov Exponent method (DLE) [35]. While displaying coherent structures or iso-surfaces, the wall of the volume can be painted with a significant scalar field.

Another simple but effective method to visualize a 3-D flow field consists in releasing a series of neutral particles and to compute numerically their trajectories integrating the following system of equations:

$$\frac{d\mathbf{x}}{dt} = \mathbf{u}\left(\mathbf{x}, t\right) \tag{5.1}$$

where $\mathbf{x}$ is the particles position and $\mathbf{u}$ is the Eulerian velocity field evaluated at the particles position. Thereafter, it is possible to display the computed trajectories color-coded with a significant scalar field, for instance the velocity magnitude.

In Figure 5.8, the trajectories of some neutral particles released on the Eulerian flow field coloured the the absolute value of the velocity are shown. In Figure 5.9 the trajectories are coloured by their mean curvature radius: this figure gives a qualitative representation of the characteristic size of the turbulence eddies.

In Figure 5.7 ECSs obtained by means of the Q-criterion are shown, while on the wall of the volume the enstropy field is drown.

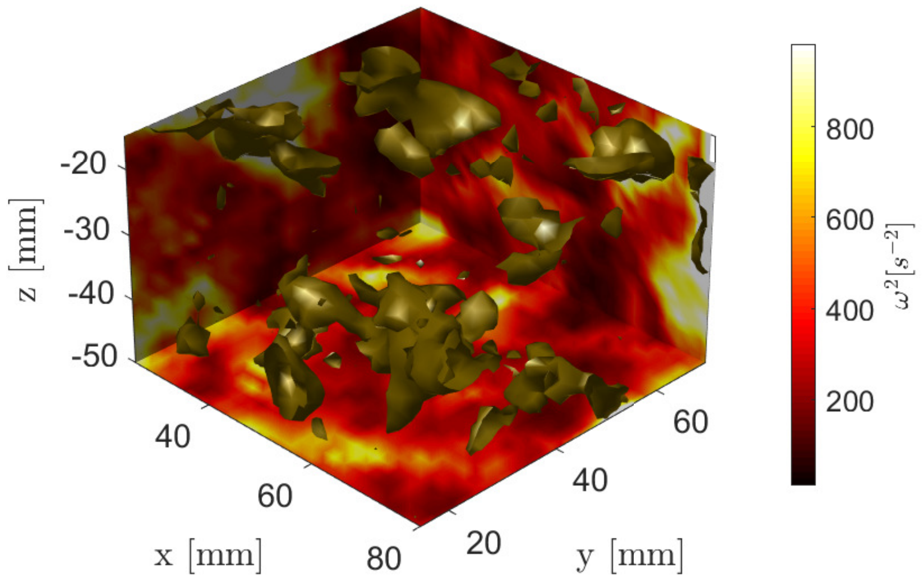

FIGURE 5.7: Visualisation of the flow field by means of ECS detected by the Q-criterion; the enstrophy field is painted on the walls.

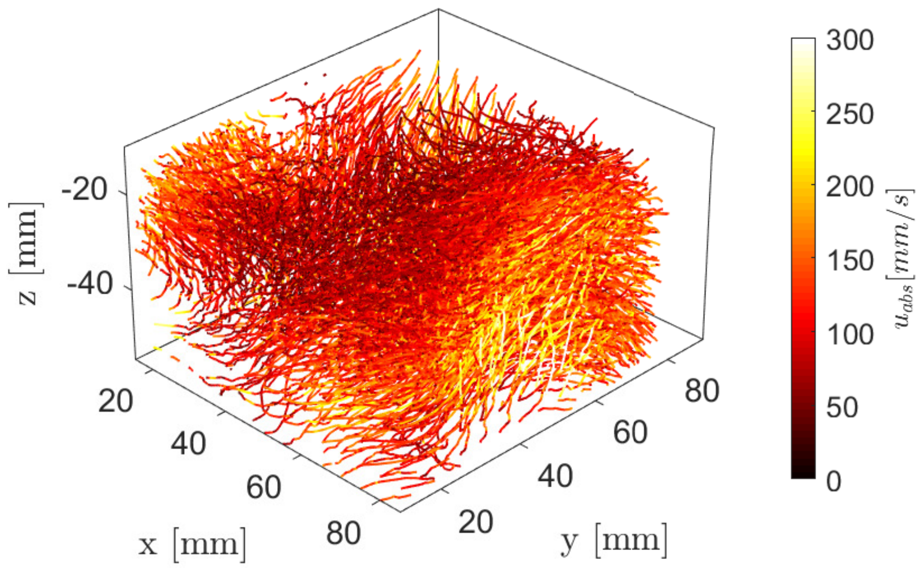

FIGURE 5.8: Particles trajectories colour coded with u_{abs}.

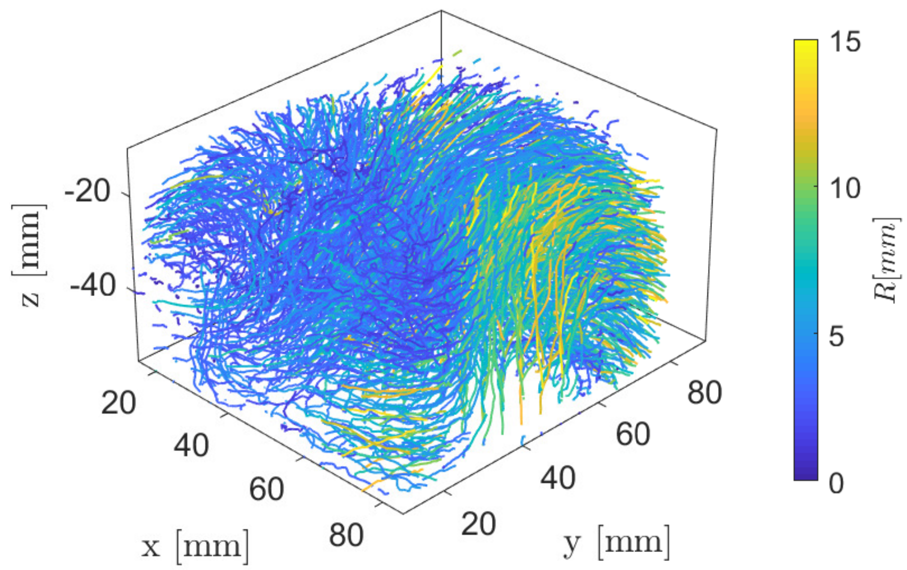

FIGURE 5.9: Particles trajectories colour coded with their ray of curvature.

5.4 3-D Fiber Tracking Velocimetry (PTV)

Two different methodology have been developed to track the the fibers position in time. The first routine consists in applying optical filters on the cameras, acting directly on the record acquisition phase. This leads to a measure of the fibers edges position without seeing the particles; the second method allows to track the fiber position and the particles simultaneously, carrying out an image pre-processing routine on a series of non filtered images.

While the first method produce an accurate description of the fiber edges velocity, the second one provide a strongly noised signal; furthermore, the second method needs a strong attention on image pre-processing parameters, so that only short time series can be analysed in a row. Notwithstanding, to have a simultaneous tracking on both the fibers and the flow can provide a qualitative representation of the fluid-structure interaction mechanisms.

Method 1: fiber edges detection with optical filters To detect only fibers, optical filters are used. As described in paragraph 5.2 the fibers are hand-crafted so that their edges are dyed with sulforhodamine b: the laser emits a light beam at a certain frequency; because the fact that sulforhodamine b is a fluorescent material, the fiber edges release light at a frequency that is different from the laser one; therefore, if the laser frequency is cut off by the optical filters, only fiber edges are visible. Nevertheless, some impurities (dust or small particles) are still visible. Since the fiber edges are particles clusters, a threshold on the pixel number is set to detect only the (bigger) fiber edges. To consider only the fibers all the couple of detected points are taken and then only the couple that are at a distance that is the fiber length are considered. Mismatch is still possible since the edges of two different fibers are separated exactly by the fiber length; nevertheless this is unlikely and it happens only for short time windows without affecting the statistics.

The calibration procedure is the same as described in the particles analysis. After the image acquisition, the tracking procedure is the same as described for particles. To ensure to consider only the fibers, a further check is carried out: all the points that are not at a distance that is the fiber length (within a tolerance) are discarded.

In order to estimate the error related to the tracking procedure, the fiber rigidity constrain is used. Indeed, in principle, the fibers end to end distance should not change. Notwithstanding, the tracking error is strong, since the size of the edges particles cluster is big as the fiber diameter. This fact leads to a high tracking error that can be estimate as the standard deviation of the fiber end to end distance.

(a) (b) (c)

FIGURE 5.10: Detail of the first camera view of three different fibers

Another constrain is given by the fact that, since the fibers are rigid, the longitudinal velocity differences should vanishes: an estimate of the error on the velocimetry measures can be given by the standard deviation of the longitudinal velocity differences. Moreover, this value can be compared with the standard deviation of the transverse velocity differences.

Figure 5.11 shows three fibers trajectories obtained by means of optical filters. No other filtering on the edges position has been used except that the standard post-processing routine described in 5.3. It can be seen that, for some time-step, the fibers seem to disappear: this is due to the strong constrains setted on the edges size: indeed, when the fibers rotate, the edges become lighter and can be cut easier by the high pass filtering procedure. This leads to have post-processed images in which the edges size is smaller that the original, and therefore the second threshold on the edges size can delete them. In order to protect from a possible data lack due to these issues, longer time series had been recorded.

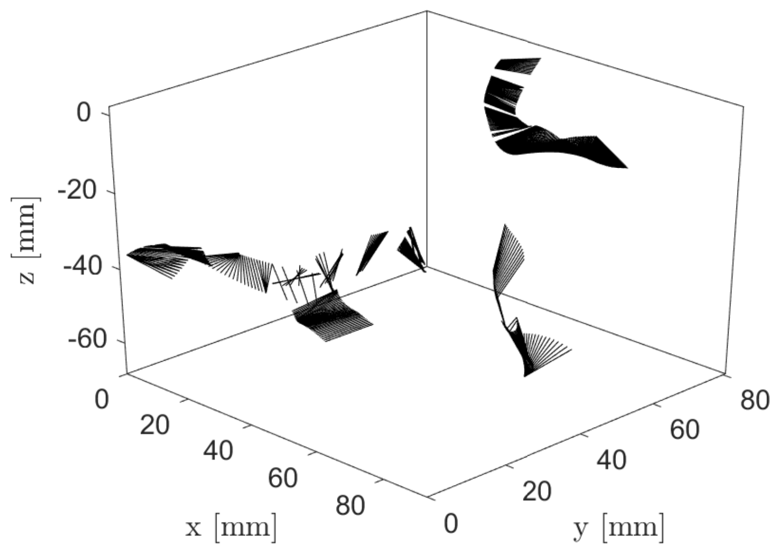

FIGURE 5.11: Trajectory of the fibers detected by means of optical filters.

Method 2: simultaneous 3-D fiber and particle tracking An alternative method to track both the fibers and the particles has been developed. Some fully dyed fibers are spread in the turbulent flow, and a record without optical filters is taken. After applying a mean filter to remove the background signal, a series of images as the one shown in Figure 5.12(a) is obtained.

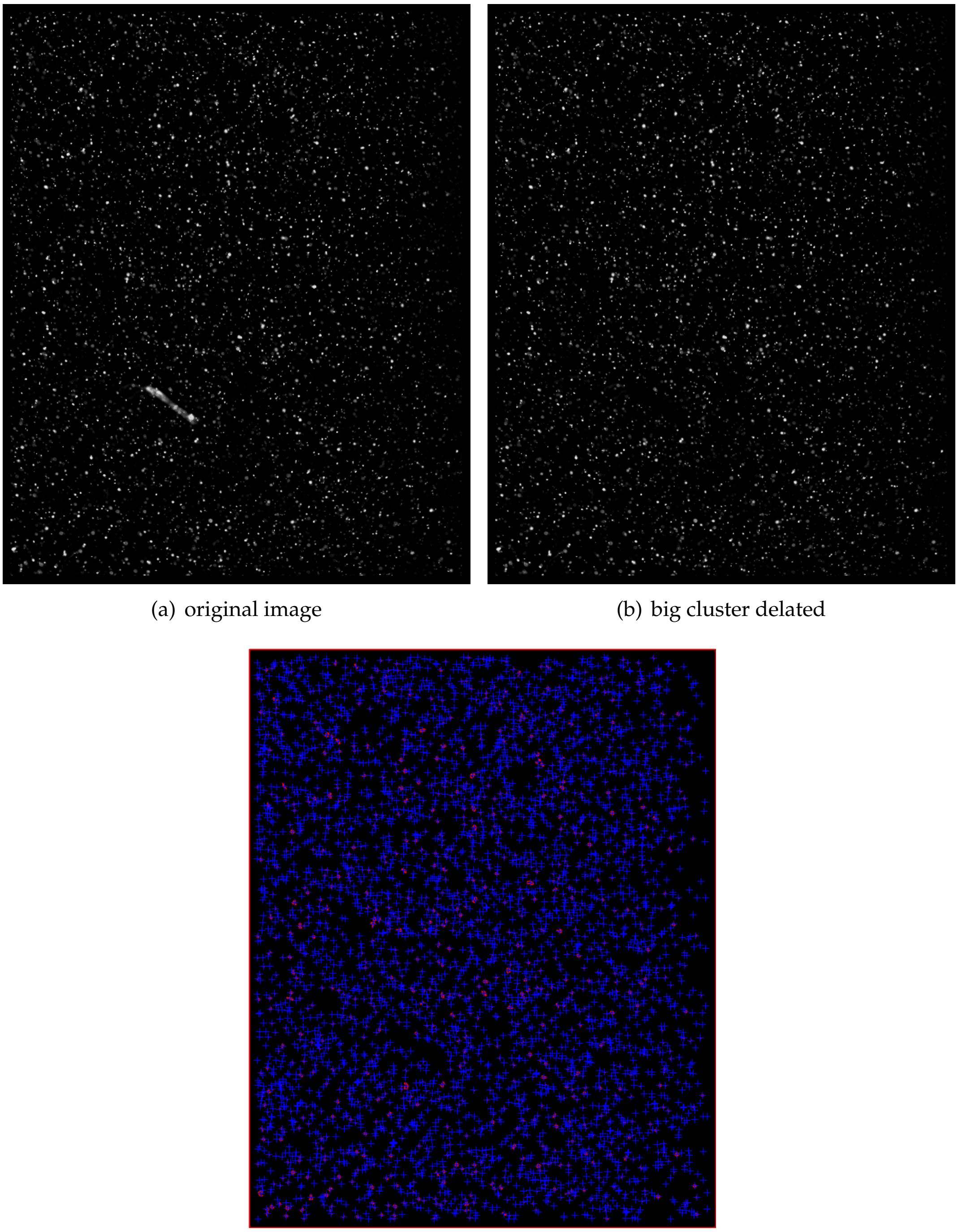

(a) original image (b) big cluster delated

(c) big cluster delated

FIGURE 5.12: Clustering procedure carried out to delete the fiber.

The images are therefore binarized in order to have a matrix on which is possible to apply a clustering routine. The size and the position of each cluster in the binary images is known and the clusters that are bigger than a threshold are discarded. Setting a proper threshold value, it is possible to delete the fibers from the image. Figure 5.12(b) is the same of 5.12(a), where the fiber has been deleted by this procedure.

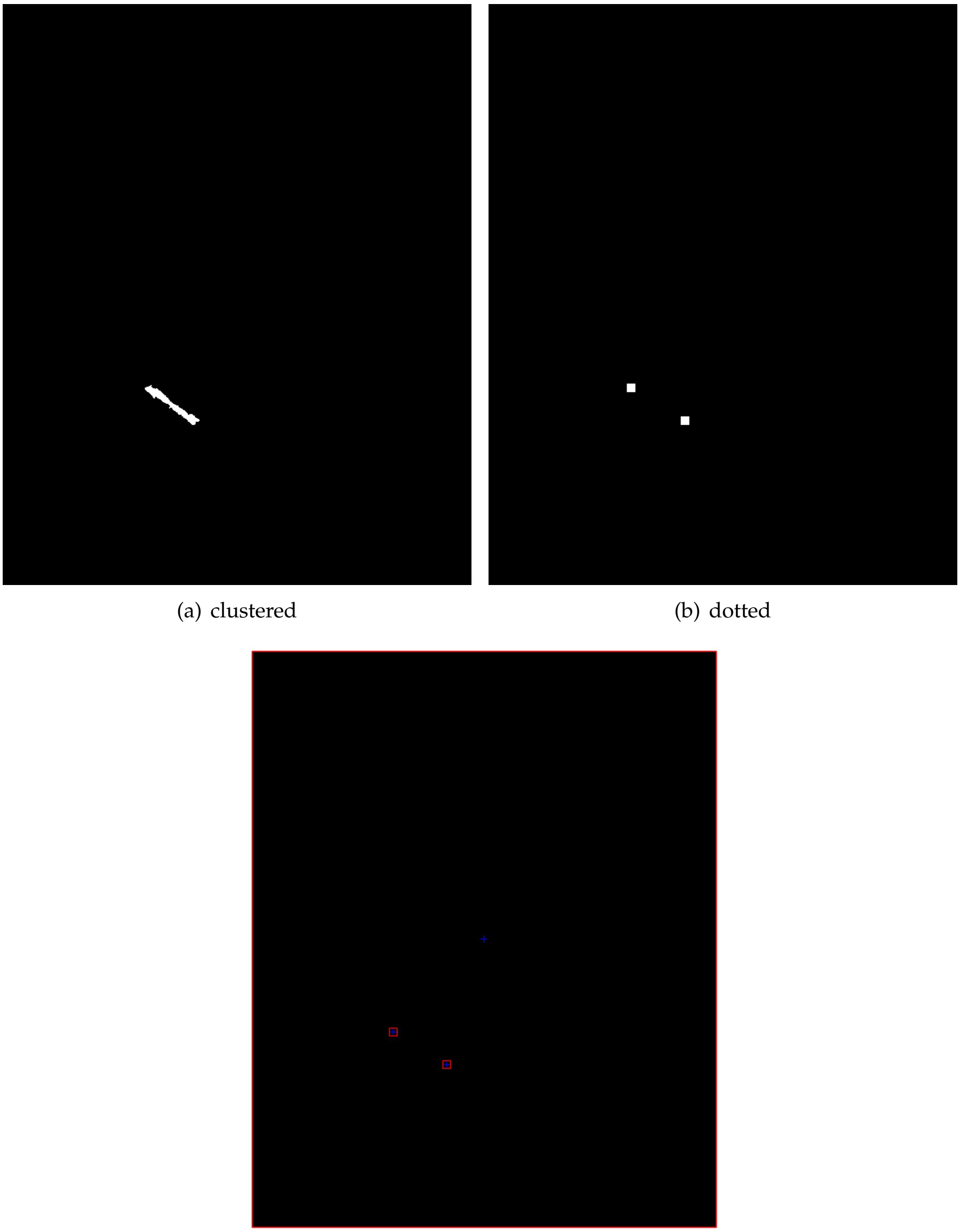

(a) clustered (b) dotted

(c) tracked

FIGURE 5.13: Automatic fiber edges detection from a non filtered image with both the particles and the fibers.

This procedure can not been carried out for long time series with the same parameters: indeed, when the fiber rotates since it is aligned with the camera main direction, the cluster size decreases and the setted threshold is to high to delete the fiber. Furthermore, if the threshold is too low, also the particles will be deleted.

Another issues of this procedure is that the algorithm incorporates in the fiber pixel cluster also the nearest particles: this leads to a leak of particles in the nearest area of the fiber surface, that is the most relevant from the point of view of the fluid structure interaction.

By applying the same procedure but keeping only the clusters bigger than a threshold, a time series of images as Figure 5.13(a) is obtained. By keeping only the farthest pixels in the images, and substituting them with two fake pixel clusters, a time series of images in which only the edges are evident is obtained (Figure 5.13(c)). Therefore, by applying the tracking procedure, the fiber edges position are obtained.

The main issue of this procedure is related to the fact that the resulting edges signal is strongly affected by noise; indeed, when the particles pass near the fiber surface, the clustering procedure merges all the pixel together. This makes the fiber cluster strongly jagged, as shown in Figure 5.13(a).

In Figure 5.14, the results of this tracking procedure is shown: it is possible to display both the fiber position and the flow filed; the same routine described in section 5.3 are carried out to visualize the flow field around the fiber. To obtain smooth trajectories, the fiber edges position have been filtered with a Gaussian kernel.

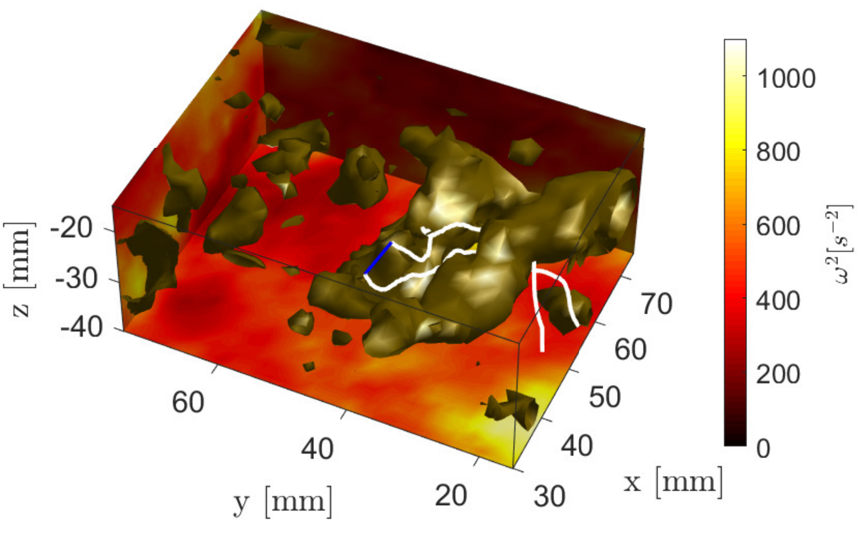

FIGURE 5.14: A rigid fiber flapping in turbulence; on the wall the enstrophy field is represented; ECS detected with the Q-criterion are displayed; the fiber is the blue line and the white tails are its edges trajectories.

5.5 Experimental routine

The experimental routine consists in four main steps that involve the techniques described before:

1. calibration procedure: the target block or calibration block, that is an object of known coordinates, is placed inside the aquarium (where the actual observation volume will be) and lighted with led light. The cameras are focused on the block and four pictures (one for each camera) are taken. Therefore the calibration parameters are estimated;

2. if the calibration error is small enough, the calibration block is removed and the turbulence generator is placed in the aquarium. The volume is illuminated with laser light and the servo motor is turned on;

3. particles are added to water with a syringe: to check if the particle density is reasonable, small recordings are taken: since it is possible to "follow" a single particle between two different time steps, the particle density can be increased;

4. a 1 *min* recording of the particles motion is taken;

5. without recalibrating the system (e.g. without removing the turbulence generator and the particles), the fibers are added to the water and the cameras are shielded with optical filters;

6. from 3 to 5 *min* recording of the fibers motion is taken;

7. all the data are processed and analysed as described in the previous sections.

An alternative routine is carried out since three different fiber length have to be investigated:

1. calibration procedure: as described before;

2. if the calibration error is small enough, the calibration block is removed and the turbulence generator is placed in the aquarium. The volume is illuminated with laser light and the servo motor is turned on; the cameras are shielded with optical filters;

3. the fibers characterized by the first length are spread in the flow filed and than a 3 *min* recording is taken;

4. the fibers are removed and the second length ones are added; the same procedure is iterate for each fiber length;

5. finally, the particles are added and the optical filters removed; a 2 *min* recording of the moving particles is taken;

6. all the data are processed and analysed as described before.

This routines are based essential on two different assumptions: firstly the turbulence has to be statistically stationary, that is that neither the mean flow nor the root mean square velocity change in time; secondly, the conditions between two different phase of the experiment do not change: this means that, for instance, by applying the optical filters, the cameras do not lose their focus; moreover, that between two different fiber lengths the calibration is still good, e.g. that the aquarium does not move.

The advantage related to the first routine is essentially that no external disturbance is done on the set-up between two different experiments. Indeed, the turbulence generator has not to be removed between two experiments. Notwithstanding, by applying this procedure, only a single fiber length can be achieved, and therefore a comparison at a unique length scale is possible. On the contrary, by using the second routine, different fiber lengths can be investigated; nevertheless, disturbance due to the movement of the turbulent generator are possible. While the first routine had been used to a preliminary investigation of the phenomena, the second had been used to investigate completely the scaling behaviour of turbulence.

Chapter 6

Results

In this chapter the main results of this project are presented. After an initial characterization of the turbulence statistical properties, a comparison between 3-D PTV and 3-D FTV results on tumbling time and transverse velocity differences is illustrated.

6.1 Flow field characterization via 3D-PTV

The statistical properties of the turbulent flow field are evaluated through 3-D particle tracking velocimetry. This flow measurement technique allows the detection of fluid particle trajectories and thus the fluid particle velocity. Furthermore, a post-processing routine discussed in [32] permits the access to the full gradient tensor along trajectories. In the following, the definition of several turbulence characteristics are presented. It has to be noticed that in order to evaluate some turbulence characteristics such as the root mean square velocity fluctuations, the integral length scale and the turbulent average dissipation rate, the particles velocities have been interpolated on an Eulerian grid.

root mean square velocity The root mean square velocity is computed through the definition in equation (2.27) where the average operator is taken over both space and time. The statistical convergence of the root mean square velocity is investigated computing this observable as a function of the sample size. Figure 6.1 shows that the u_{rms} convergence profile exhibits a rather high initial fluctuation which is probably due to data lack. After a transitional phase in which the profile increases steadily ($\sim 2 \cdot 10^5$ data-points), the bumps are reabsorbed and the statistics converges.

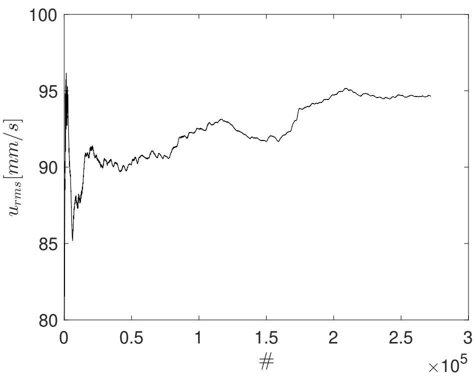

FIGURE 6.1: Root mean square velocity as a function of the sample size.

average turbulent dissipation rate In this work, the turbulent average dissipation rate is estimated through the approximation shown in equation (2.33). Indeed, the estimation of the average turbulent dissipation rate by its definition (2.25), requires a high resolution of the flow field that can capture the lower scales of the energy spectrum. On the contrary, if the resolution of the measurements is not high enough, the higher spatial gradients connected to the smaller scales are smoothed, therefore it is not possible to observe local changes related to the smaller scales. Since the average turbulent dissipation rate term acts at the smallest scales of the energy spectrum (high wave numbers), a low resolution of flow field strongly affects its evaluation by means of its definition, resulting in an under-estimation of ϵ.

The flow field resolution is formally time and space dependent, since particles move and cluster. Notwithstanding, to have an impression of the resolution, a proxy can be obtained by the following equation:

$$d = \left(\frac{V_{observation\,volume}}{\langle n_{particles}\rangle}\right)^{1/3} \sim \left(\frac{70 \cdot 80 \cdot 30\, mm^3}{3000}\right)^{1/3} = 4.21\, mm \tag{6.1}$$

Comparing this value with the probability density function of the separation distance between all the couples of tracked particles (Figure 6.2) it can be seen that the probability to observe couples at a distance lower than 4.21 mm is significantly low. It

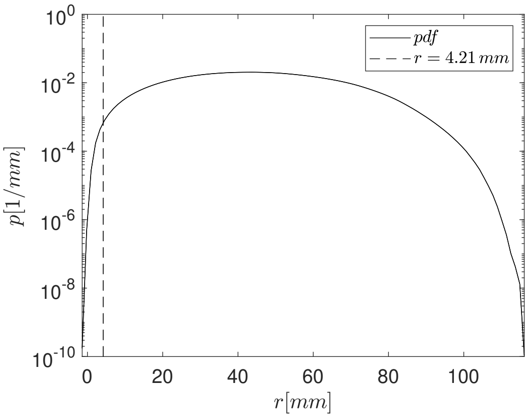

FIGURE 6.2: Probability density function of the separation between the tracked particles.

is clear thus that the resolution of the flow field is not high enough to allow a proper estimation of the turbulent dissipation rate. Nevertheless, since the production balances the dissipations, the average turbulent dissipation rate can be also estimated from the root mean square velocities and the integral length scale (2.33). This expression is useful when the flow field resolution is not sufficiently accurate. In our case, since a large volume has to be investigated, the particle density is not high enough to measure properly space gradients; thereafter, 2.33 is used to evaluate the dissipation rate.

Another possible technique to evaluate the turbulent dissipation rate is to interpolate the 4/5 law (2.30). In Figure 6.6(a), the longitudinal third order moment is compared with the 4/5 law where ϵ has been evaluated independently balancing production and dissipation. As can be seen, a good accordance between the two evaluation methods can be observed.

integral length scale The integral length scale can be evaluated as the integral of the averaged space autocorrelation function, defined as:

$$L = \int_0^\infty C(r)\,dr, \quad C(r) = \left\langle \overline{\mathbb{E}\left[\frac{u'(\mathbf{x}) \cdot u'(\mathbf{x}+\mathbf{r})}{u'(\mathbf{x})^2}\right]} \right\rangle \tag{6.2}$$

where $\mathbf{r}$ is a space increment. To determine $C(r)$, for each time-step an ensemble of random segment of fixed length is extracted from the volume; then, the signal of one of the velocity components is evaluated along this segment. The auto-correlation of this signal is taken and then the average both over space and time is computed (Figure 6.3). Since L depends slightly on which segments are taken (that is a random choice), only the order of magnitude is considered. Moreover, a good check for L can be done observing Figure 6.6(b) and 6.6(a): here, the size of the separation r that does not follow any more the scale $4/5$ scale low is expected to be of the same order of the integral length scale evaluated with (6.2).

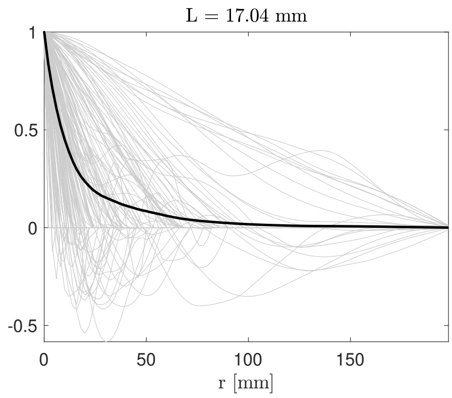

FIGURE 6.3: Space autocorrelation function averaged over space and time.

micro-scales From the turbulence average dissipation rate, the Kolmogorov and the Taylor microscales as well as the Reynolds number of the Taylor micro-scale are evaluated as in (2.37), (2.38), (2.39) and (2.41), (2.40).

The main turbulence statistical properties are listed in Table 6.1 and 6.2: the turbulent dissipation rate is evaluated balancing the production and the dissipation, whereas the integral length scale is evaluated as shown in Figure 6.3.

$u_{rms}\,[mm\,s^{-1}]$	$L[mm]$	$T\,[s]$	$Re_L\,[-]$
94.65	15.00	0.1585	1420

TABLE 6.1: Flow integral properties.

$\epsilon\,[m^2\,s^{-3}]$	$\eta\,[mm]$	$\tau_\eta\,[s]$	$u_\eta\,[mm\,s^{-1}]$	$\lambda\,[mm]$	$Re_\lambda\,[-]$
0.0565	0.065	15.47	0.0042	1.54	145.93

TABLE 6.2: Flow micro scales.

6.2 Velocity differences

The velocity differences are evaluated directly from the Lagrangian trajectories: for each time-step, all the possible particles couples are considered and the separation vector $\mathbf{r}$ as well as the velocity difference vector $\delta\mathbf{u}$ are calculated. Thereafter, the longitudinal ($\delta u_{\|}$) and transverse ($\delta u_{\perp}$) projection of $\delta\mathbf{u}$ on $\mathbf{r}$ are evaluated for each couple of fluid particles as described in Section 2.4.

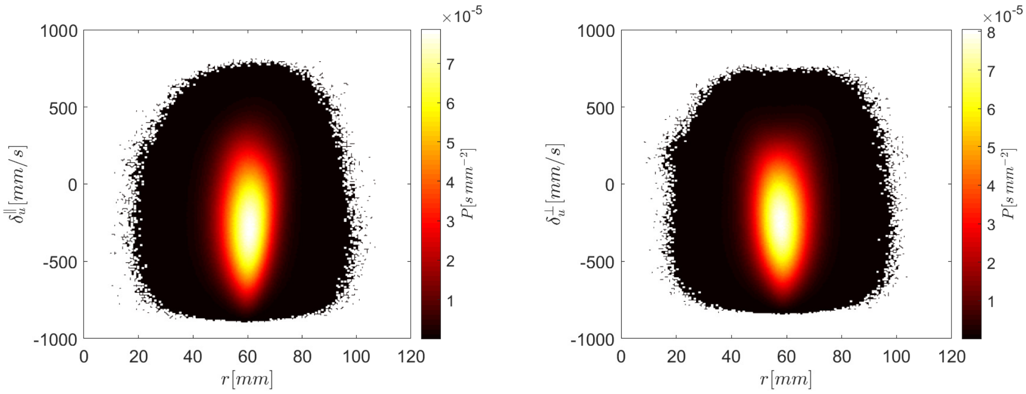

(a) longitudinal direction

(b) transverse direction

FIGURE 6.4: Joint pdf of the velocity differences evaluated from the particle trajectories.

probability density functions In Figure 6.4, the joint probability density functions of $\delta u^{\|}$ (Figure 6.4(a)), $\delta u^{\perp}$ (Figure 6.4(b)) and r are presented.

Here, as well as in the other jpdfs in the thesis, the bin size was obtained automatically by means of the function *hist2* (MATLAB®), which provides an optimal trade-off between the bin size and the amount of available data by means of a V-fold cross validation procedure (see [36]).

AS can be seen from Figure 6.4, there is a rather high probability to observe particles couples separated by a distance $r \sim 60\,mm$. This means that, convergence problems at the smaller scales can be encountered. As it will be shown below, although the integral scale is significantly smaller (about $15\,mm$), it is still possible to have converged statistics inside the inertial range.

To obtain the mono-variate empirical probability density functions as the ones shown in Figure 6.5, the optimal trade-off between the bin size and the amount of data is obtained automatically by means of the function *ksdensity* (MATLAB®) that implement a k-density algorithm.

In Figure 6.5, the normalized probability density functions of the particles at the length-scale of the fibers are shown; by normalizing the velocity differences with the square root of their second order moment, a perfect accordance between the three pdfs should be observed, except for extreme events that are the tails of the distribution. This discrepancy between the PDFs of the velocity differences is usually called intermittency and it is commonly observed in 3-D turbulence. More in details, the intermittency consists of infrequent strong bumps in the time velocity signal measured in a fixed point of a turbulent field when a high-pass filter is applied; the higher the pass frequency, the more frequent the bumps appear. An efficient way to appreciate this phenomenon is to focus on the tails of the pdfs: if the pdfs built for different values of the separations are scaled with their standard deviation, a strong difference in the tail behaviour has to be observed while r is decreased. Another valuable method that can be used to observe the intermittency is to evaluate the higher order even moments of these pdf: accordingly to K41 theory, these moments should follow a power law of $r^{p/3}$, where p is the moment order. However, it is well-known in the turbulence literature the existence of a deviation of the data form these moments, because of the intermittency effect [18, Ch. 8]. Notwithstanding, intermittency seems not to be present by looking at Figure 6.5. We can not observe an intermittent behaviour as the separation reduces because the collected data does not provide enough resolution at the smallest scales to have converged statistics.

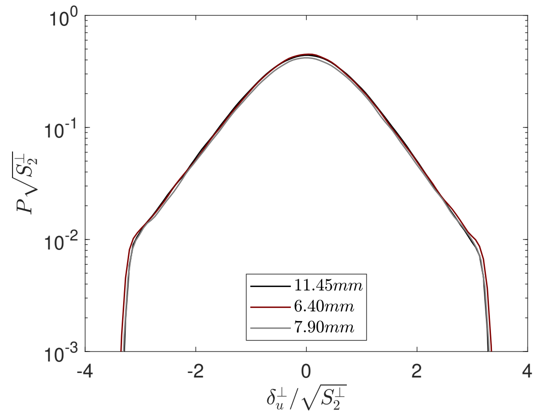

FIGURE 6.5: pdf of the transverse velocity differences evaluated with particles at the length scales of the fibers.

structure functions The observables related to a fixed value of the separation $|\mathbf{r}|$ are evaluated averaging the value within the interval $[|\mathbf{r}| - dr, |\mathbf{r}| - dr]$, where dr can be chosen as small as possible, in order to have a good trade off between the structure functions smoothness and the random sampling. To make this concept more clear, the schematic procedure is described in the following:

1. the dataset is shuffled randomly;
2. a small certain bin width (dr) is chosen;
3. two structure functions are built: one with the first half of the dataset and the second with the other part;
4. if dr is too small the two structure functions will be completely different and really unstable, e.g. very scattered;
5. the bin width is increased;
6. the procedure starts again from point 1 and repeated until the two structure functions are equal within an error.

This algorithm provides a good criterion to find an optimal trade-off of the kind of the well known bias variance decomposition ([37]). This approach is used in the field of density estimation, which is a common problem in the Machine learning which consists in building empirical probability density function from data without supervision and without preliminary assumption about the statistical model.

In Figure 6.6(a) the scale laws for the second and the third order moments of the longitudinal velocity differences are shown; in both cases, the data follows rather well the curves of the power law $r^{p/3}$ within the limit of the inertial range ($r < L \sim 15\,mm$). In particular, the longitudinal third order structure function represents the skewness of the probability density function of the longitudinal velocity differences. As can be seen from Figure 6.6(a), this function exhibits more relevant convergence problems. Indeed, this function converges by data deleting, and a higher amount of data is needed for its convergence. In any case, the classical negative values predicted by the K41 theory are captured. Furthermore, for the third order longitudinal structure function, the dissipation are calculated independently and no curve fitting procedure has been carried out. The $\frac{4}{5}\epsilon$ coefficient fits very well the power law.

In Figure 6.6(b), the transverse second order structure function is presented. As can be seen, for a large range of the separation distance, our data collapse very well on the the well known $r^{2/3}$ law within the inertial range for values of r/L smaller than the unity.

As expected, for the scale equal or bigger than L in all the showed structure functions, the well known Kolmogorov power laws are not respected any more, that means that the turbulence at this scales is not freely decaying.

Since the Kolmogorov 4/5 law has been derived for an ideal turbulence scenario, the accordance between the scale laws and the experimental data (that are not nether isotropic or homogeneous but only stationary) is due to fact that the turbulence field recreated is locally ideal; in fact this means that the mean flow gradients are slowly variant, e.g. the gradient related to the mean flow are far weaker than the local and instantaneous gradient related to the turbulent fluctuations: the variations of the mean flow acts on a scale that is greater than the integral length scale.

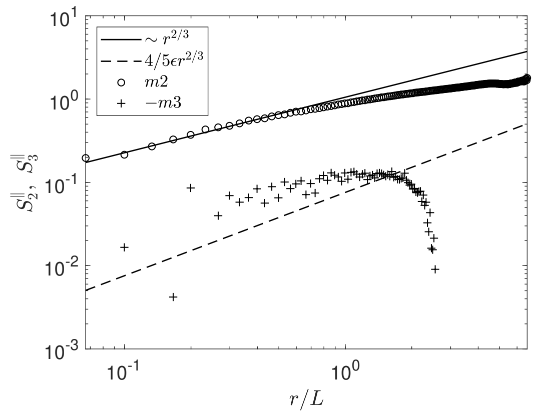

(a) second and third order, longitudinal

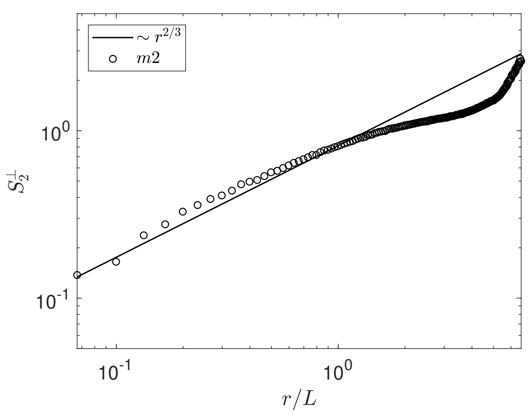

(b) second order, transverse

FIGURE 6.6: Structure functions; length and velocities are adimensionalized with the integral scale and the root mean square velocities.

6.3 Comparison between fibers and particles

In the following a comparison between the transverse velocity increments computed by means of tracer particles and rigid fibers is presented. Here the transverse velocities are evaluated as discussed in the section 2.

More in detail, for each time step of the PTV output, all the possible particle couples are evaluated. Among these particle couples only for those at a fixed distance (within a tolerance), the velocity increments $\delta\mathbf{u}$ are computed. In FTV the only separation distance available is the fiber length. Given their rigidity, the longitudinal velocity differences of their edges is almost zero. It is also worth to note that for a single fiber length it is possible to evaluate only single point on the $S_2^\perp$, which is $S_2^\perp\ (r = c)$ where c is the fiber length.

probability density functions In Figure 6.7, the probability density functions of the transverse velocity differences evaluated both with particles and fibers at three different separation distances is presented. Here, in order to avoid non-convergence problem in the density estimation, some extreme events were discarded removing data characterized by too low probability in a first rough estimation. As can be seen from these three pdfs, the FTV and the PTV data provide very similar results. A minor difference between the two methods in the negative tail of the pdf of the intermediate fiber length can be noted.

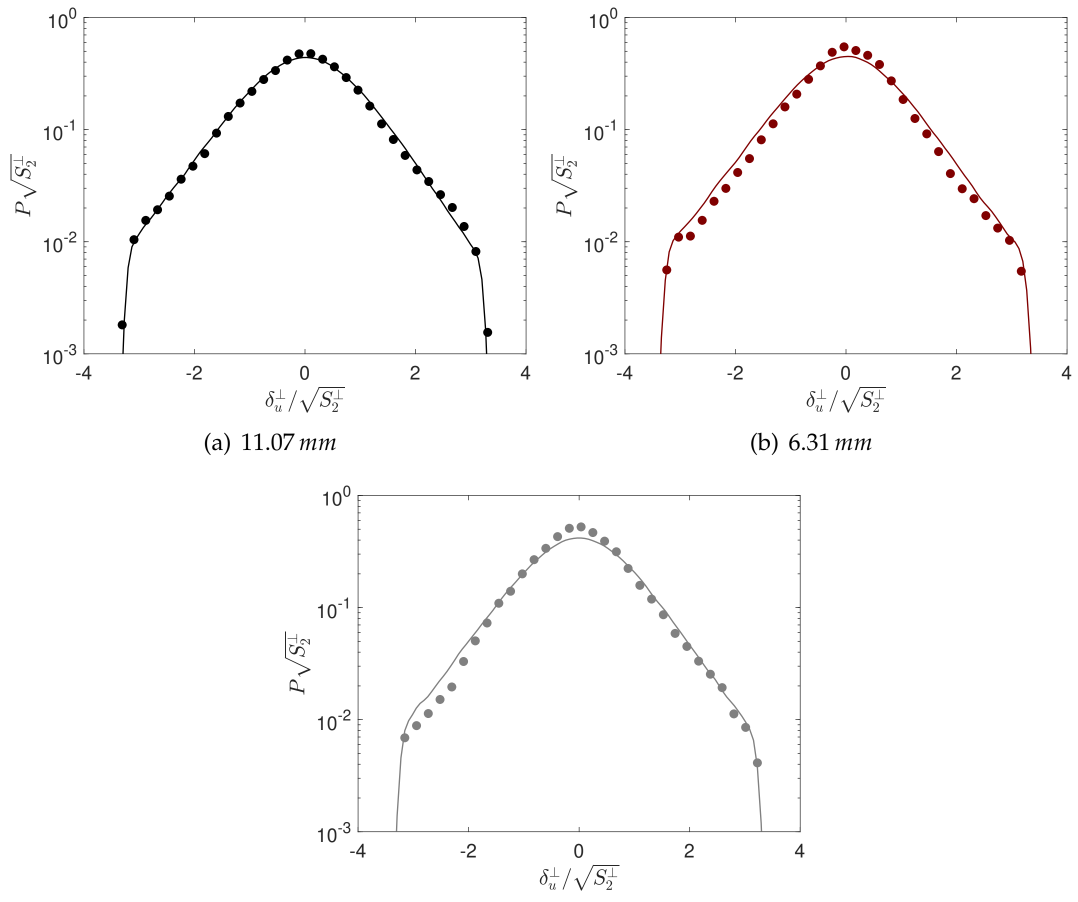

(a) 11.07 mm

(b) 6.31 mm

(c) 7.84 mm

FIGURE 6.7: pdf of the transverse velocity differences evaluated both PTV and FTV; the distributions are normalized with the variance of the particles velocity differences.

second order structure function In Figure 6.8, the second order structure function of the transverse velocity differences, evaluated both with particles and fibers, is shown. Here,the fibers, are represented by the three red points. Again the results from the FTV show a very good accordance with the PTV data. The results from the both techniques scale with the 2/3 power of the separation distance, as predicted by the Kolmogorov theory. Nevertheless, the longest fiber shows a better accordance with the particles at its length scale. On the plot, there are shown also the errorbars of points evaluated with the fibers. Not surprisingly, the errorbars are too small to be visualized. This means that there are no appreciable errors related to convergence problems: indeed, a large amount of data is available.

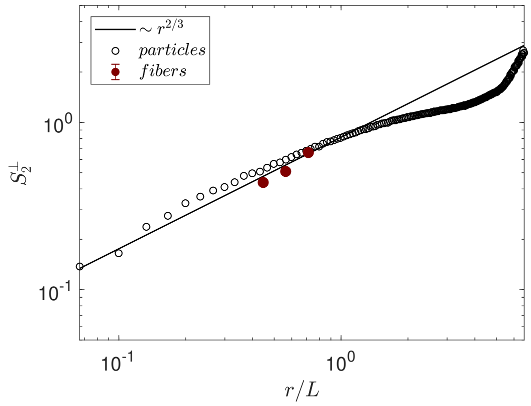

FIGURE 6.8: Second order transverse structure function evaluated both with fibers and particles; length and velocities are made dimensionless with the integral scale and the root mean square velocities.

Kolmogorov constant The Kolmogorov constant is evaluated as shown in (2.53). This constant represents the best fitting of the scale power law of the scale of the power law with exponent 2/3. Ideally, both the black circles and the red bullets should be constant at different r/L, with $r/L < 1$. Figure 6.9 shows more clearly that the best description of the second order scale law is given by the longer fiber that is characterized by a smaller value of the aspect ratio.

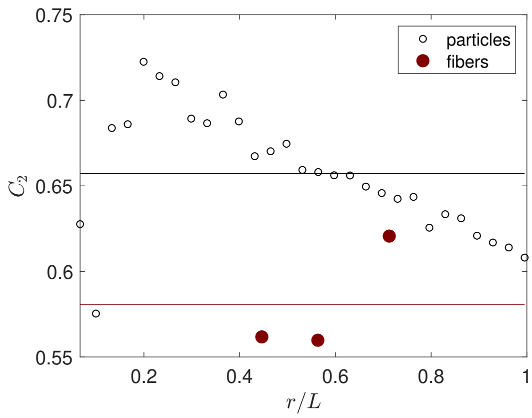

FIGURE 6.9: Kolmogorov constant.

convergence profiles of the second order moment In Figure 6.10 the convergence profiles of the second order moment of the transverse velocity differences evaluated with the fibers are shown. No substantial differences can be appreciated in all the cases. No convergence problem are present. To have a good convergence of the second order moment, it is necessary to use $\sim 2 \cdot 10^4$ data points, that means, considering our frame-rate ($400\, fps$), $\sim 50\, s$. The width between the errorbars (red solid lines), are evaluated as:

$$error = \max\left(S_2^{\perp}\,(\#)\right) - \min\left(S_2^{\perp}\,(\#)\right) \tag{6.3}$$

considering # to be within the last 1/5 of the data sample. From these results it is clear that no convergence issues are present. Therefore, the small discrepancies between the second order moments evaluated with fibers and particles are due purely to physical reason that are discussed later.

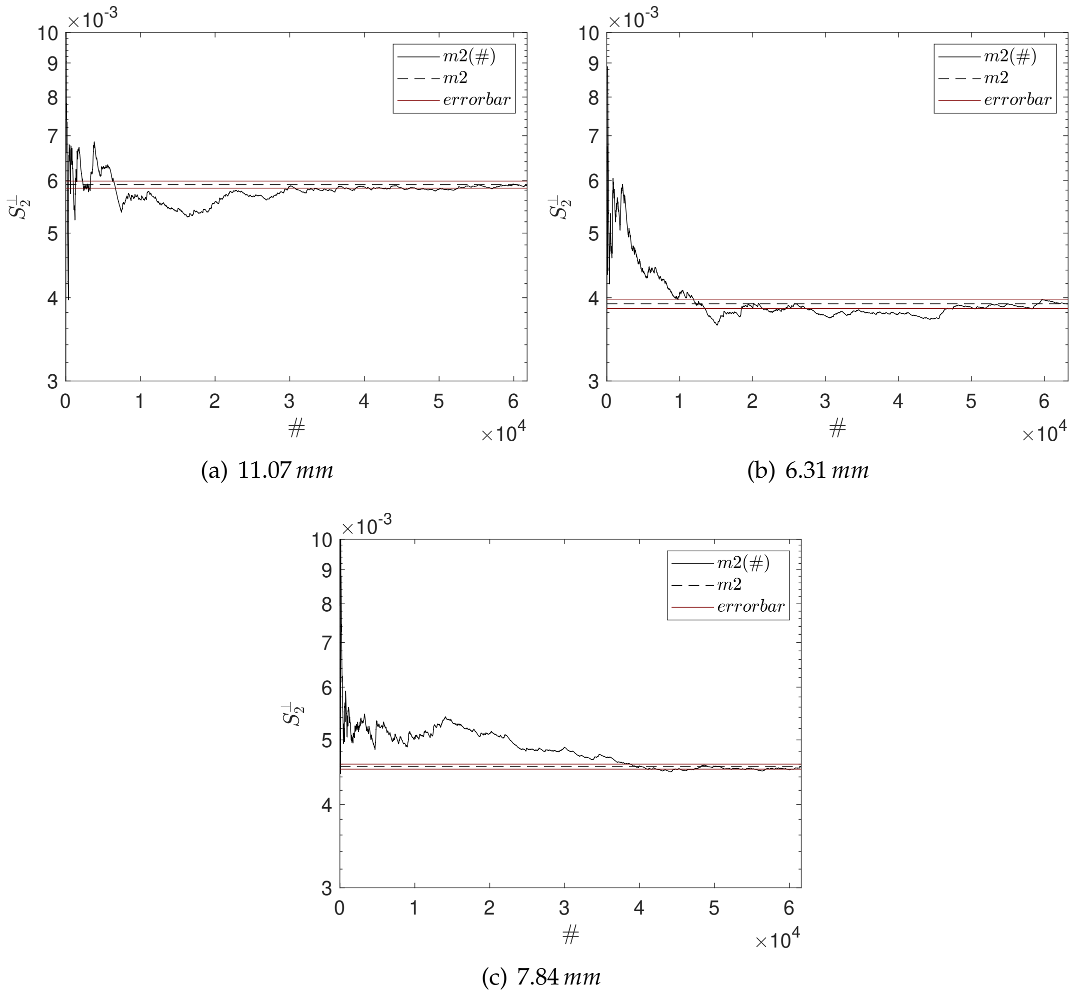

(a) $11.07\, mm$

(b) $6.31\, mm$

(c) $7.84\, mm$

FIGURE 6.10: Convergence profile of the second order moment for the three different fibers.

tumbling time In Figure 6.11, the so called tumbling time evaluated through the FTV is presented. Here the tumbling time is evaluated as described in section 3.3 and compared with the Kolmogorov scale law (equation (2.35)). Again, surprisingly an almost perfect accordance between the results from the FTV and the Kolmogorov theory can be noticed. Such results constitute an extremely encouraging proof of the possibility of using FTV techniques for the turbulent flows description and characterization.

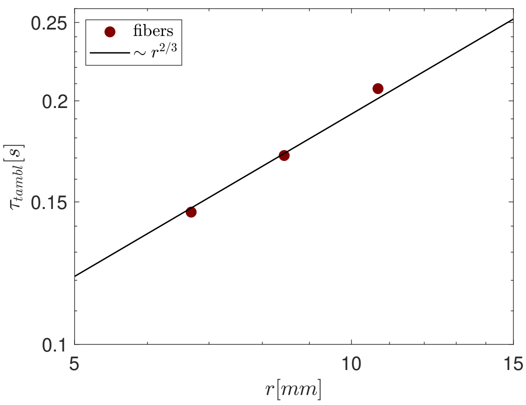

FIGURE 6.11: Tumbling time measured with the three fibers.

Chapter 7

Discussion and further steps

In this thesis, a new optical technique, the so-called Fibers Tracking Velocimetry (FTV), for flow measurements was introduced and tested. This technique has some similarity with the well-known Particle Tracking Velocimetry (PTV) in that both techniques reconstruct particle trajectories. However, if the PTV technique aims to reconstruct the fluid particle trajectories of neutrally buoyant flow tracers, the FTV consists in tracking the two edges of a 1-D rigid element (fiber), that can, and usually does, not follow the local fluid flow. More interestingly, it was shown that by measuring the velocity at the edges of the fibers, it is possible to reconstruct the second order moment scale law of the transverse velocity differences that is in very good accordance with PTV data. Furthermore an estimation of the fiber tumbling time matches the eddies turn-over time at the scale of the fiber length.

7.1 Fibers measure the transverse velocity increments and the eddies turn-over time

Figure 6.7, 6.8 and 6.9 show clearly that is possible to obtain an estimation of the transverse velocity difference by means of rigid fibers instead of particles. The second order structure function constant $C2$ is slightly underestimated using the fibers ($\sim 10\%$). Figure 6.11 shows a perfect accordance between the tumbling time of the fibers and the Kolmogorov $2/3$ law up to a constant factor: this fact can be tricky; indeed, since the turbulence scenario is not ideal, it is possible that the $2/3$ scale law can be not followed by the turbulent flow.

Nevertheless, given that the scaling constants for different turbulent flow scenarios are well-known, it is possible to have an indirect estimation of the other scaling constants, such as the Kolmogorov C_2 constant for the second order longitudinal structure function (indeed it can be obtained by equation (2.52)) or the turbulent diffusivity of a passive scalar field.

7.2 The rotational Stokes number affects the fiber dynamic

A rather significant adversity of using the FTV is related to the difficulty of obtaining rigid fibers characterized by low Stokes numbers. In fact, as shown in figure Figure 6.9 the aspect ratio of the fibers plays a crucial role on the characteristic Stokes number of the fiber. In particular St increases with the aspect ratio of the fiber (3.1). Since, in our study, the diameter of the fibers cross-section is somehow limited by their hand-crafting technique, the only free parameter is their length. Therefore, the lower the fiber length is, the less the fiber follows the flow. Moreover, comparing Figure 6.7(a) with the Figures 6.7(b) and 6.7(c), it can be seen that the main differences between the pdfs of the transverse velocity difference between fibers and particles are related to the stronger positive or negative velocity differences. This observation is probably due to the fact that the faster the flow field around an object (i.e. the fiber), the higher is the instantaneous Stokes number related to that forcing. At the state of the art it is not possible to have a direct experimental measure of the rotational or translational Stokes number of a rigid fiber, but the observation above discussed about the fibers behaviour can be seen as a proxy of the fact that the Stokes number is increasing with the aspect ratio with the same trend as expected by the slender body theory.

Notwithstanding, even if the differences between the shorter fibers and the flow behaviour are probably due to the different fiber length (bigger Stokes number), the possibility to observe discrepancy because of the non stationary of the phenomena is still present. This problem can be fixed in future experiments using three of the four cameras to look at the fiber motion, and a fourth camera with an image splitter (that is a system of mirrors that makes four points of view out of a single camera) to look at the flow field in the same experiment: this is one of the step forward that I would like to achieve in the next months; it is also useful to understand how the fiber motion influence the instantaneous flow field.

7.3 Further questions and possible experiments

A list of other questions and possible new experiments that that can further improve the work presented in this thesis is provided in the following:

floating fibers can measure free surface turbulence? A range of floating fibers characterized by different lengths can be spread on the free surface of a turbulent flow, such as an open channel flow or a tidal pool. Then the surface turbulence can be estimated by means of PIV technique to have a reliable characterization of the surface flow field; therefore it is possible to make a 2-D track of the fiber position and measure, for instance the tumbling time or the transverse velocity increments with both the methods. The fibers are expected to tumble at the same frequency of the eddies of their length scale;

how does the Stokes number affect the fiber flapping behaviour? With the same set-up and fiber casting methods of our work, it is possible to increase the Stokes number, changing the fluid properties (adding ethanol to increase the viscosity), changing the fiber properties (changing the inertia of the fibers changing the material properties), and increasing as much as possible the turbulent intensity, and thus the root mean square velocity; doing so, it should be possible to observe that the pdf of the velocity differences evaluated with the particles and the fibers is different; also, analysing a wide range of cases, it should be possible to see in which limits of the Stokes number it is possible to measure the transverse velocity differences;

real life frexible fibers Both with human hairs or nylon sting it should be possible to investigate the flexible case that has been already investigated by direct numerical simulations; such an experiment could be feasible within the Holzner lab at ETHZ.

meso-scale experiments A rather interesting and useful experiment at meso-scale could be thought within the oceanographic environment: a system composed by two surface floats connected with a rope that can be laid down on the ocean surface. The system can be designed such that the rope is rolled up on one of the floats and can be released in a controlled manner. In this way, several separation distances can be achieved with a single system. For instance, by means of a remote control, or with a timed system, the rope is released after some large eddy turnover time, i.e. an amount of time sufficiently large for the statistics to converge. With such a procedure one can build an estimation of the scale laws of interest within the inertial range.

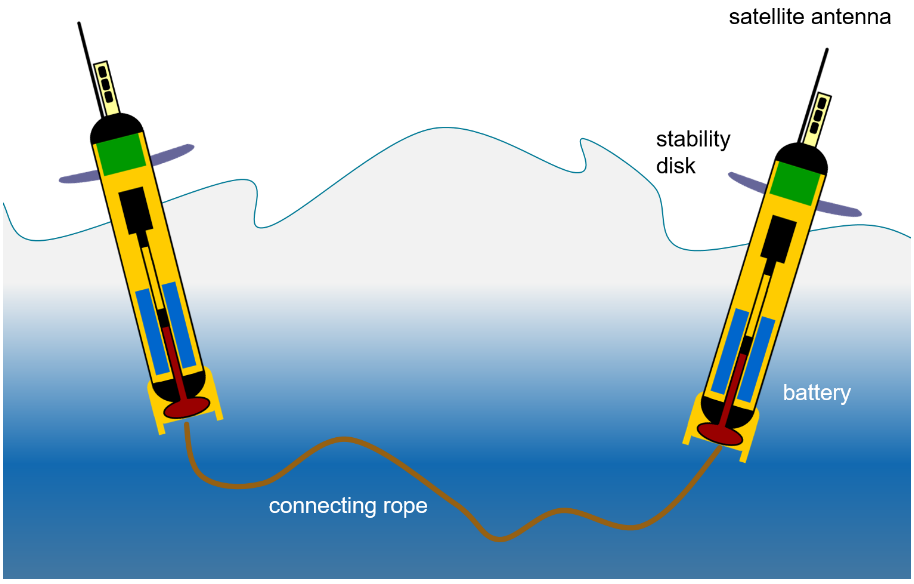

FIGURE 7.1: Scheme of two oceanographic drifters connected with a rope.

an assembly of freely moving rigid fibers measures the flow velocity gradient tensor? As shown in [38],for sufficiently small Stokes times of the assembly, the flow velocity gradient tensor can be reconstructed by tracking the fiber assembly and measuring suitable fiber velocity differences evaluated at the fibers edges; a feasible experiments can be designed by means of small closed loop pumps (flow rate $\sim$ $10 - 200\, ml/s$) and PDMS made channels; keeping the channel and the flow rate size small enough, it is possible to create a quasi 2-D sheared laminar flow and to measure the the position of the edges of the fibers by means of a single camera recording and a 2-D particle tracking algorithms.

Bibliography

[1] M. Liu, J. Sun, Y. Sun, C. Bock, and Q. Chen, "Thickness-dependent mechanical properties of polydimethylsiloxane membranes," *Journal of micromechanics and microengineering*, vol. 19, no. 3, p. 035028, 2009.

[2] G. K. Batchelor, "The application of the similarity theory of turbulence to atmospheric diffusion," *Quarterly Journal of the Royal Meteorological Society*, vol. 76, no. 328, pp. 133–146, 1950.

[3] W. K. Melville, F. Veron, and C. J. White, "The velocity field under breaking waves: coherent structures and turbulence," *Journal of Fluid Mechanics*, vol. 454, pp. 203–233, 2002.

[4] J. C. Wyngaard, *Turbulence in the Atmosphere*. Cambridge University Press, 2010.

[5] L. Chamorro, C. Hill, S. Morton, C. Ellis, R. Arndt, and F. Sotiropoulos, "On the interaction between a turbulent open channel flow and an axial-flow turbine," *Journal of Fluid Mechanics*, vol. 716, pp. 658–670, 2013.

[6] J. L. Aragón, G. G. Naumis, M. Bai, M. Torres, and P. K. Maini, "Turbulent luminance in impassioned van gogh paintings," *Journal of Mathematical Imaging and Vision*, vol. 30, no. 3, pp. 275–283, 2008.

[7] U. Gülan, B. Lüthi, M. Holzner, A. Liberzon, A. Tsinober, and W. Kinzelbach, "Experimental study of aortic flow in the ascending aorta via particle tracking velocimetry," *Experiments in fluids*, vol. 53, no. 5, pp. 1469–1485, 2012.

[8] D. B. Chelton and M. G. Schlax, "Global observations of oceanic rossby waves," *Science*, vol. 272, no. 5259, pp. 234–238, 1996.

[9] Z.-S. She and E. Leveque, "Universal scaling laws in fully developed turbulence," *Physical review letters*, vol. 72, no. 3, p. 336, 1994.

[10] M. Nelkin, "Universality and scaling in fully developed turbulence," *Advances in physics*, vol. 43, no. 2, pp. 143–181, 1994.

[11] W. Schmidt, C. Federrath, and R. Klessen, "Is the scaling of supersonic turbulence universal?," *Physical Review Letters*, vol. 101, no. 19, p. 194505, 2008.

[12] H. Maas, A. Gruen, and D. Papantoniou, "Particle tracking velocimetry in three-dimensional flows," *Experiments in fluids*, vol. 15, no. 2, pp. 133–146, 1993.

[13] T. Rossby, "Evolution of lagrangian methods in oceanography," *Lagrangian Analysis and Prediction of Coastal and Ocean Dynamics*, pp. 1–38, 2007.

[14] L. F. Richardson, "Atmospheric diffusion shown on a distance-neighbour graph," *Proceedings of the Royal Society of London. Series A, Containing Papers of a Mathematical and Physical Character*, vol. 110, no. 756, pp. 709–737, 1926.

[15] J. LaCasce, “Statistics from lagrangian observations,” *Progress in Oceanography*, vol. 77, no. 1, pp. 1–29, 2008.

[16] M. E. Rosti, S. Olivieri, A. A. Banaei, L. Brandt, and A. Mazzino, “Flowing fibers as a proxy of turbulence statistics,” *Meccanica*, pp. 1–14, 2018.

[17] M. E. Rosti, A. A. Banaei, L. Brandt, and A. Mazzino, “Flexible fiber reveals the two-point statistical properties of turbulence,” *Physical review letters*, vol. 121, no. 4, p. 044501, 2018.

[18] U. Frisch and A. Kolmogorov, *Turbulence: the legacy of AN Kolmogorov*.

[19] J. Paret and P. Tabeling, “Experimental observation of the two-dimensional inverse energy cascade,” *Physical review letters*, vol. 79, no. 21, p. 4162, 1997.

[20] S. B. Pope, “Turbulent flows,” 2001.

[21] E. Lévêque and A. Naso, “Introduction of longitudinal and transverse lagrangian velocity increments in homogeneous and isotropic turbulence,” *EPL (Europhysics Letters)*, vol. 108, no. 5, p. 54004, 2014.

[22] A. Noullez, G. Wallace, W. Lempert, R. Miles, and U. Frisch, “Transverse velocity increments in turbulent flow using the relief technique,” *Journal of Fluid Mechanics*, vol. 339, pp. 287–307, 1997.

[23] R. Benzi, L. Biferale, G. Paladin, A. Vulpiani, and M. Vergassola, “Multifractality in the statistics of the velocity gradients in turbulence,” *Physical review letters*, vol. 67, no. 17, p. 2299, 1991.

[24] J. Herweijer and W. Van de Water, “Transverse structure functions of turbulence,” in *Advances in Turbulence V*, pp. 210–216, Springer, 1995.

[25] S. Kurien and K. R. Sreenivasan, “Anisotropic scaling contributions to high-order structure functions in high-reynolds-number turbulence,” *Physical Review E*, vol. 62, no. 2, p. 2206, 2000.

[26] B. Dhruva, Y. Tsuji, and K. R. Sreenivasan, “Transverse structure functions in high-reynolds-number turbulence,” *Physical Review E*, vol. 56, no. 5, p. R4928, 1997.

[27] S. Chen, K. R. Sreenivasan, M. Nelkin, and N. Cao, “Refined similarity hypothesis for transverse structure functions in fluid turbulence,” *Physical review letters*, vol. 79, no. 12, p. 2253, 1997.

[28] C. Duprat and H. A. Shore, *Fluid-Structure Interactions in Low-Reynolds-Number Flows*. Royal Society of Chemistry, 2015.

[29] C. S. Peskin, “Flow patterns around heart valves: a numerical method,” *Journal of computational physics*, vol. 10, no. 2, pp. 252–271, 1972.

[30] N. Quennouz, M. Shelley, O. Du Roure, and A. Lindner, “Transport and buckling dynamics of an elastic fibre in a viscous cellular flow,” *Journal of Fluid Mechanics*, vol. 769, pp. 387–402, 2015.

[31] J. Willneff, “A spatio-temporal matching algorithm for 3d particle tracking velocimetry [phd dissertation],” *Zürich (Switzerland): Swiss Federal Institute of Technology Zurich*, 2003.

[32] B. Lüthi, A. Tsinober, and W. Kinzelbach, "Lagrangian measurement of vorticity dynamics in turbulent flow," *Journal of Fluid mechanics*, vol. 528, pp. 87–118, 2005.

[33] G. Boffetta, G. Lacorata, G. Redaelli, and A. Vulpiani, "Detecting barriers to transport: a review of different techniques," *Physica D: Nonlinear Phenomena*, vol. 159, no. 1-2, pp. 58–70, 2001.

[34] J. C. Hunt, A. A. Wray, and P. Moin, "Eddies, streams, and convergence zones in turbulent flows," 1988.

[35] M. A. Green, C. W. Rowley, and G. Haller, "Detection of lagrangian coherent structures in three-dimensional turbulence," *Journal of Fluid Mechanics*, vol. 572, pp. 111–120, 2007.

[36] P. Hall, S. J. Sheather, M. Jones, and J. S. Marron, "On optimal data-based bandwidth selection in kernel density estimation," *Biometrika*, vol. 78, no. 2, pp. 263–269, 1991.

[37] P. Domingos, "A unified bias-variance decomposition," in *Proceedings of 17th International Conference on Machine Learning*, pp. 231–238, 2000.

[38] M. Cavaiola, S. Olivieri, and A. Mazzino, "The assembly of freely moving rigid fibers measures the flow velocity gradient tensor," *arXiv preprint arXiv:1908.04072*, 2019.